Master's Thesis

Design and Measurement of Spoof Plasmon Resonators for Microwave Index Sensing

Yeon Soo Lim

Department of Materials Science and Engineering

Graduate School of UNIST

2020

Design and Measurement of Spoof Plasmon Resonators for Microwave Index Sensing

Yeon Soo Lim

Department of Materials Science and Engineering
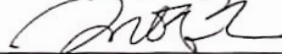
Graduate School of UNIST

Design and Measurement of Spoof Plasmon Resonators for Microwave Index Sensing

A thesis/dissertation

submitted to the Graduate School of UNIST

in partial fulfillment of the

requirements for the degree of

Master of Science

Yeon Soo Lim

12. 04. 2019

Approved by

Advisor

Young Chul Jun

Design and Measurement of Spoof Plasmon Resonators for Microwave Index Sensing

Yeon Soo Lim

This certifies that the thesis/dissertation of Yeon Soo Lim is approved.

12/04/2019

_____

Advisor: Prof. Young Chul Jun

_____

Prof. Gang Il Byun : Thesis Committee Member #1

_____

Prof. Eun Mi Choi : Thesis Committee Member #2

Abstract

Surface plasmons (SP) are generated by the interaction between electromagnetic (EM) waves and conduction electrons on the surface of conductive materials. SPs are usually observed in the optical or near-infrared region. On the other hand, in the lower frequency regime such as microwave or terahertz range, SP modes do not exist because the field cannot penetrate into metals. To overcome this limitation, metamaterials based on corrugated metal patterns were introduced, which are called spoof SPs. Spoof SPs show similar properties to optical SPs. Especially, spoof localized SPs (LSPs) can confine EM waves near compact resonant structures (like LSPs in metal nanoparticles), and they can be applied to sensing. In this thesis, we report on the fabrication of spoof LSPs on a photopaper using inkjet printing and conduct the microwave measurements of spoof LSP resonances. In addition, we show the ability of spoof LSPs for microwave index sensing. In single or coupled resonator structures, we measure how the resonance frequencies and intensities change upon the index variation. We expect spoof LSP structures could be useful for IoT sensors because of simple and cheap fabrication and easily tunable resonance frequencies.

Contents

List of Figures

Figure 3.11 Index sensing test using coupled structure with the Vernier effect. **(a)** Illustrations that explain experimental conditions according to the sensing elements. Arrangement of source and detectors is described, which are already introduced in Figure 3.9. In all cases, on right resonator, sensing elements are fixed with $f.f._2 = 0$ (left column) or 0.6 (middle column) or 1 (right column), while elements on left ($f.f._1$) are changing. **(b)** Results of sensing experiments. Frequency ranges are zoomed in near hexapole resonance. **(c)** Analysis of hexapole resonance peaks in (b). Left y-axis with black color represents resonance frequency, right y-axis with red color |S21| and x-axis $f.f._1$. Doted lines denote largest |S21| value for each cases. **(d)** Illustrations explaining the frequency shifts, where the largest intensity peaks occur in each case. Blue, orange, purple lines correspond to the larger, smaller resonator and coupled structure, respectively. For each case, bold lines correspond to where resonance peaks are overlapped.

1. Introduction

Surface plasmon(SP) is the interaction between electromagnetic(EM) waves and free electrons on the surface of conductive material [1]. The excited free electrons collectively oscillate and form polaritons. When dielectric material and metal have same magnitude but opposite signs (Re(ε) < 0 for metal; Re(ε) > 0 for dielectric material) of permittivity at the resonance frequency [2, 3], SP is excited at the interface of dielectric material and conductive material. There are two kinds of the SP. *Surface plasmon polariton*(SPP) propagates on the flat surface of metal and is confined within subwavelength region (Figure 1.1 (a)), while *localized surface plasmon*(LSP) excited by the metal subwavelength sized nanoparticles (usually noble metal) arising naturally from scattering (Figure 1.1 (b)) [4]. Although LSPs can't propagate (unlike SPP), they do not require phase matching techniques so can be excited by direct light illumination. Restoring forces cause electrons to polarize, which results in plasmon oscillation confined within the nanoparticle.

The best-known property of the surface plasmon is the confinement of light near the surface, an effect for which there are several applications-e.g., nearfield microscopy [5], biomedical sensing [6, 7], nanophotonic [8], optoelectronics [9], photovoltaics [10] and nanoantenna[11]. In addition, the easy excitation of LSP has led to the development of many sensors exploiting LSP. The study of refractive index sensing according to nanoparticle size (Figure 1.2 (a)) [12], the invention of fluorescence microscopy employing strong field confinement between two nanoparticles (Figure 1.2 (b)) [13], and the research of bio-molecule sensing with gold nanoparticles decorated with targeting agents (Figure 1.2 (c)) [14] have all followed from the discovery of this exciting property.

(a)   (b)
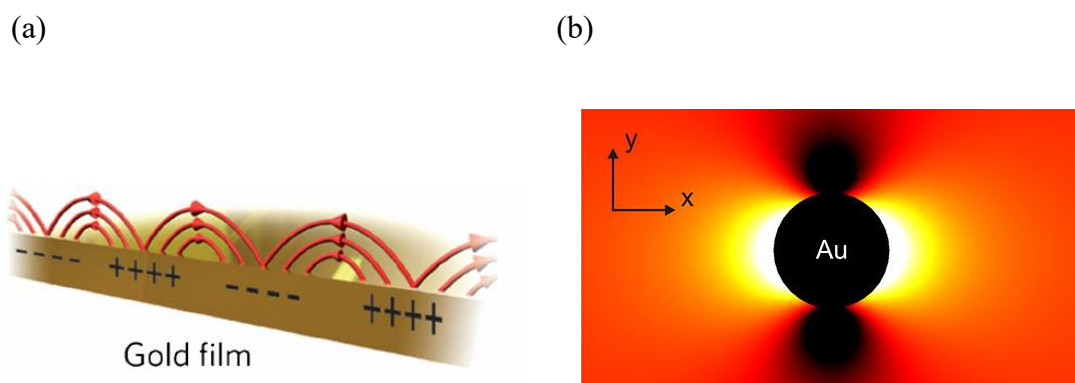
Figure 1.1 Two kinds of Surface Plasmon. **(a)** Surface Plasmon Polariton (SPP) at flat metal surface. **(b)** Localized surface Plamon (LSP) at metal nano particle. Reproduecd from [4].

(a)

(b)

Au Nanospheres   Au Nanocubes

(c)

Surface binding
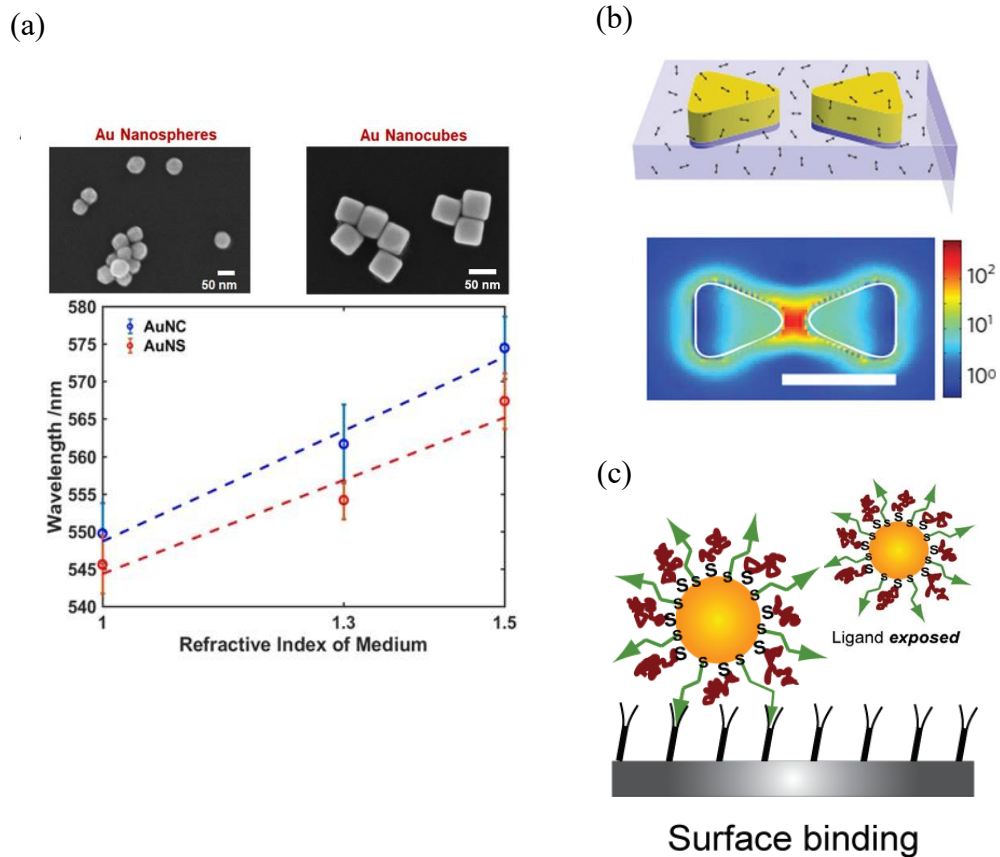
Figure 1.2 Examples of LSP sensors. **(a)** Refractive index sensing. Reproduced from [12]. **(b)** Fluoresence microscopy. Reproduced from [13]. **(c)** Bio-molecule sensing. Reproduced from [14].

The preceding phenomena are confined to the optical region. For SP excitation, EM waves need to penetrate into the metal although SP originates from the loss of the metal which results in degenerated confinement. On the other hand, in regions of lower frequency, EM waves are shielded due to the prompt reaction of free electrons by the incident EM waves (Figure 1.3 (a)) compared to optical frequency range (Figure 1.3 (b)). Thus, metals are regarded as a perfect electric conductor(PEC) in GHz or THz region[15]. Instead, only Zenneck surface wave can support confined, bound EM modes on flat metal surface. However, due to insufficient penetration depth, EM waves are weakly bounded [16]. For EM waves to penetrate the metal, we exploited metamaterial, artificially structured materials that exibit properties not found in nature [17]. By introducing grooves on the metal surface with geometric parameters smaller than wavelength, as in Figure 1.3 (c), the structures are treated as an homogenous but anistropic configuration and can be described as an effective medium approximation. This strategy enables EM waves to be confined and support SP mode near the metal surface structure by erroneously positing that EM can penetrate into the metal.
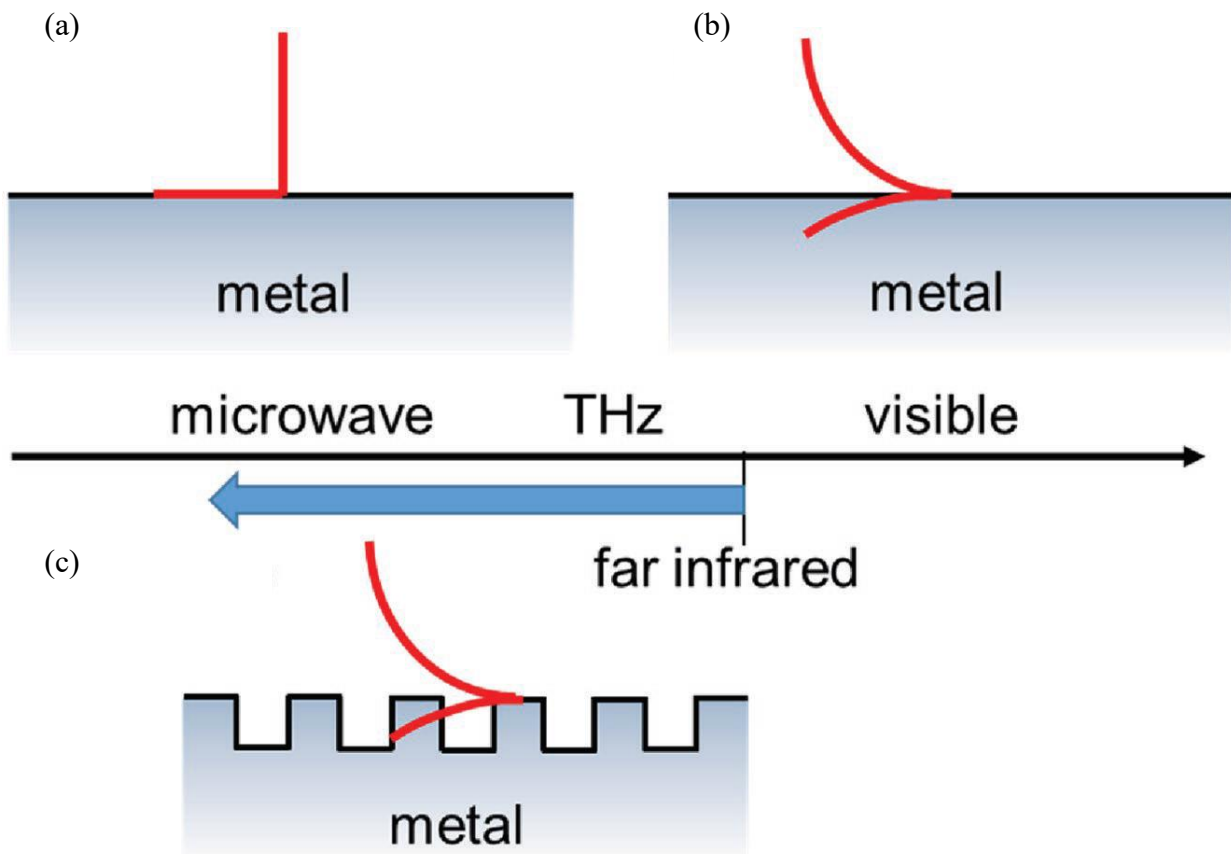
Figure 1.3 EM field confinement at different frequency ranges. **(a)** EM wave incident on flat metal surface at microwave range. Zenneck surface waves are supported. **(b)** Incident on flat metal surface at visible range. SPPs are confined. **(c)** Incident on grooved metal surface from microwave to far infrared range. Confined EM, that is spoof SPP, is supported. Reproduced from [35].

The first concept for SP in PEC limit was proposed by Pendry et. al [18]. Their metastructure was a 2D array of holes perforated in PEC metal. They proved that the EM field can be bound to the surface of the structure by the Drude model with effective medium approximation. They found the dispersion relation was similar to optical SP. Furthermore, they claimed that 1D corrugated structures could also support SP mode like the optical region [19]. The close similarity to SP in optical frequency led to bound EM mode in the PEC structure, which is called *Spoof surface plasmon*. Eventually, by the spoof SP, it could be possible to bring the SP from optical frequency to microwave or THz frequency. Since then, spoof SPPs have been studied through various theoretical approaches, such as numerical solution, modal matching approach, effective medium method [20-24]. In these articles, they used 1D structures with not perfectly but partially perforated holes. Conformal SPP waves then emerged in a very thin structure with corrugated metallic strips, which inspired the appearance of compact or ultrathin designs at micro- and terahertz region [25-27]. Thin structure is more advantageous for fabrication, so spoof SPP waveguides have been subject to much studies [28-30]. Spoof SPP can propagate on the flexible substrate or bent lines, as described by Figure 1.4 (a), and its propagating property has been confirmed [25, 31]. Wireless body sensor cloth using spoof SPP was introduced quite recently, (see Figure 1.4 (b) [32]). In this article, subjects wore the cloth on which spoof SPP waveguides combined with body sensors were attached and then the responses from their bodies were studied.

(a)   (b)

Figure 1.4 Applications of spoof SPPs. **(a)** Spoof SPP waveguides on flexible film. Reproduced from [25]. **(b)** Spoof plasmon textiles for wireless body sensor. Reproduced from [32].

A few years after the appearance of spoof SPP, spoof LSP also appeared in 2012 by *A. Pors et al.* [33]. By arranging 1D grooves circularly, they constructed a cylinder with infinitely long corrugated grooves, proving that spoof LSP can be supported by the structure. Unit cells of the spoof LSP originated from the spoof SPP because the corrugated cylinder could be achieved by bending flat grooved metal circularly as illustrated by Figure 1.5. Dispersion relations can thus be shared between the spoof SPP and LSP in the corrugated 1D structure [34], and the corrugated metal cylinder is comparable to the nanoparticles that excite LSP at optical frequency range.

In the spoof LSP structure, waves propagate along the perimeter of the cylinder or disk so multipole resonances are excited as a form of standing wave when integer times of the LSP wavelength is equal to the perimeter [35]. To realize spoof LSP in the real world, ultrathin metal structures were also studied in the spiral structure supporting magnetic resonance [36]. Finally, X. Shen et al. experimentally demonstrated ultrathin spoof LSP (Figure 1.6 (a)) [37]. Since then, spoof LSP were also followed by many studies with not only the corrugated form, but also spiral (Figure 1.6 (b)), ring resonator with double corrugations, MIM ring resonator [38-40]. In addition, coupled structures have also been studied between LSP elements according to a variety of gaps (Figure 1.6 (c)) and even propagating spoof LSPs like waveguide were realized along several elements [41-45].

Like the optical LSP, due to the strong EM wave confinement, the advantages of spoof LSPs are to be applied to the sensors. Moreover, resonance frequency tuning and higher order resonance excitation just by simply altering the structural factors boost the merits [46, 47]. Because working frequency for each sensor can be adjusted without difficulties and the more sensitivity of higher resonances will help to fabricate elaborate sensors. These properties make spoof plasmon as a good candidate for sensors and there are several articles related to spoof LSP sensing experiment (Figure 1.6 (d)) [37, 48-51].

bending Spoof SPP

Spoof LSP   **Nanoparticle**
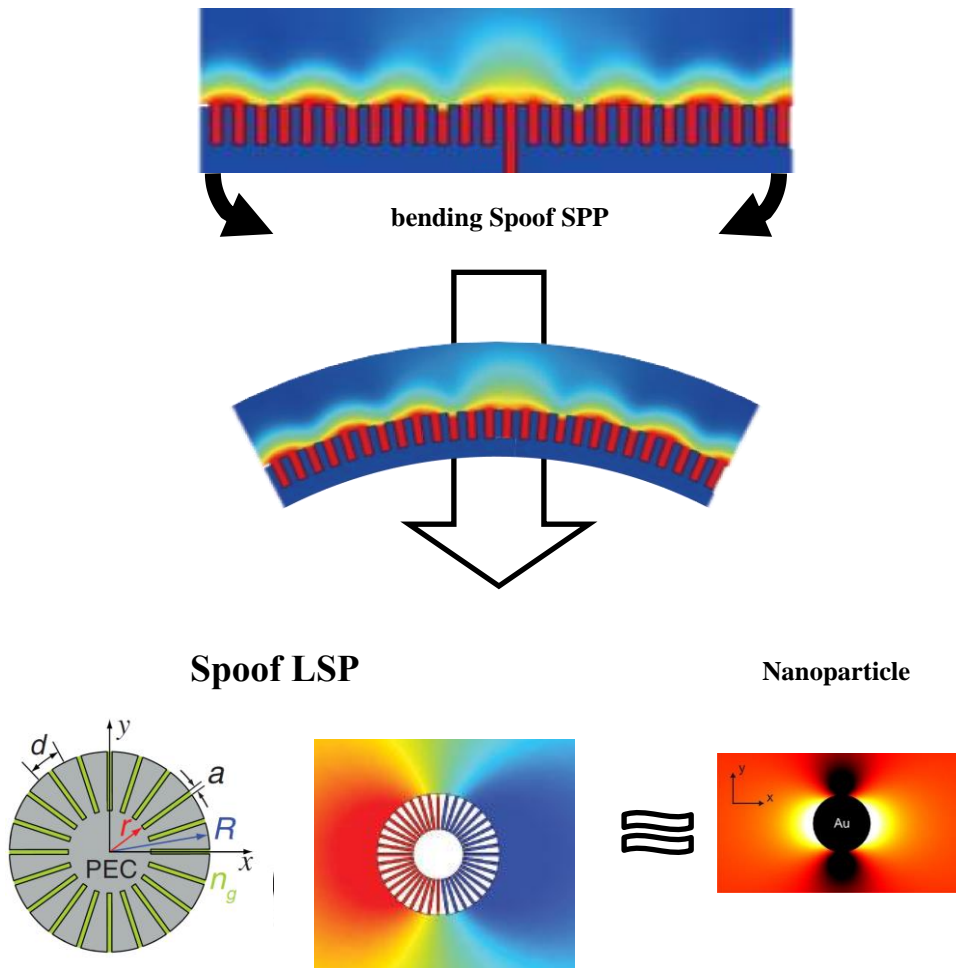
Figure 1.5 Spoof LSP (bottom left) can be achieved by bending flat metal grooves circularly that support spoof SPP (top and middle). Adapted from [24,34]. Spoof LSP is comparable to the nanoparticle (bottom right) at optical frequency. Reproduced from [4].

(a)

(c)

(b)

(d)
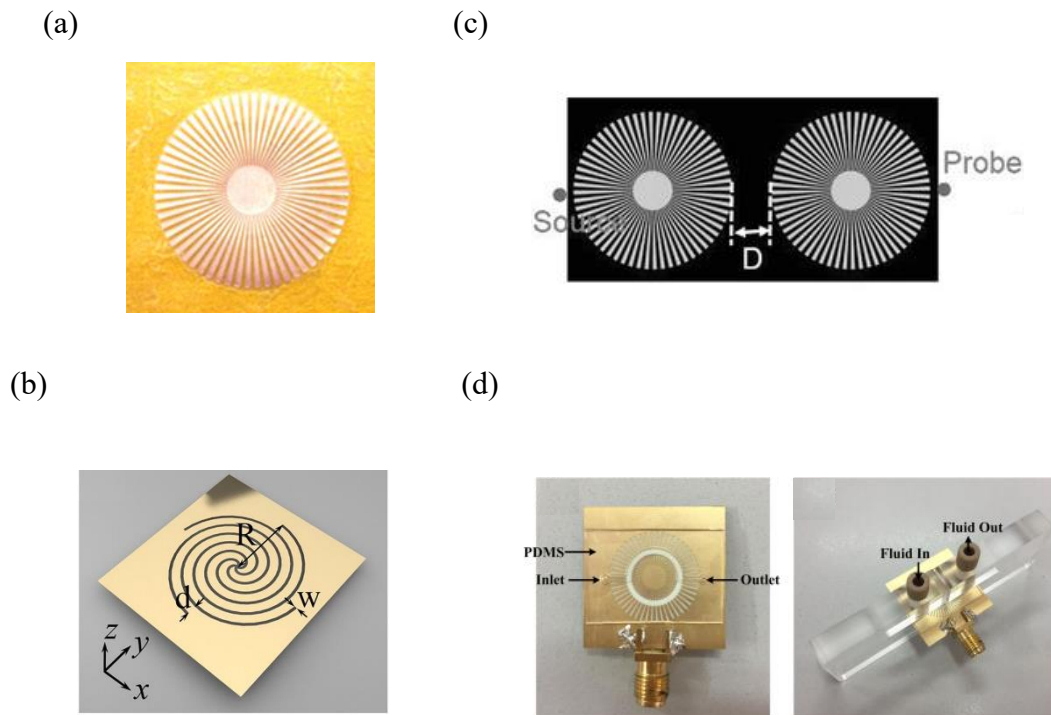
Figure 1.6 Examples of spoof LSPs. **(a)** Picture of fabricated ultrathin spoof LSP resonator. Reproduced from [37]. **(b)** Spiral shaped spoof LSP resonator. Reproduced from [39]. **(c)** Coupled structure with gap = D between two spoof resonator. Reproduced from [45]. **(d)** Spoof LSP resonator for microfluidic chemical sensor. Reproduced from [49].

It has been important to bring the SP from optical to GHz frequency range. Since the advent of 5G communication, many everyday items can connect to the Internet or mobile phone well known collectively as the Internet of Things (IoT). The frequency band of 5G communication ranges from a few GHz to one hundred GHz according to each device, and 5G mobile communications use around 28GHz [52]. Because spoof plasmons can cover this frequency range, they offer themselves as a powerful tool for 5G communications. Strongly confined fields in which sensitive signals change in response to the circumference condition would be a clue for IoT sensors. Furthermore, the easy frequency tuning of spoof SP would help to match appropriate working frequency according to each product.

Among many fabrication techniques, inkjet printing is one of the most popular and familiar method. These days, many articles use inkjet printers to easily fabricate optical elements with metallic ink on a variety of substrates [53-55]. Although certain properties like conductivity are worse in inkjet printing than lithography or the printed circuit board (PCB) method, inkjet printing is nevertheless fast, affordable, simple to use and consumes less material than these counterparts. Also, because the geometry parameters of spoof LSPs are mm size within few GHz range, commercial printers are sufficient to fabricate resonators.

Within optical frequency range, there are many sensors to which Vernier effect is applied [56-58]. Vernier effect is coupling of two structures, illustrated by Figure 1.7 [59]. The top graph with red color is a result of a reference with fixed frequency periods, and the middle, black chart describes the sensing part, where frequency periods slide in response to the sensing object. In the coupled structure at the bottom of the blue figure, overlapping peaks between the reference and sensing parts are filtered and others are suppressed. This concept is usually applied to the sensors by analyzing these periodic and sharp peaks. Spoof LSP structures have several resonances. So, by combining Vernier effect with spoof LSP, we can filter resonance peaks. It seems unlikely that spoof LSP with Vernier effect has been studied. So, using this effect, multiple index sensing or complex signals can be realized at the coupled spoof LSP structures.
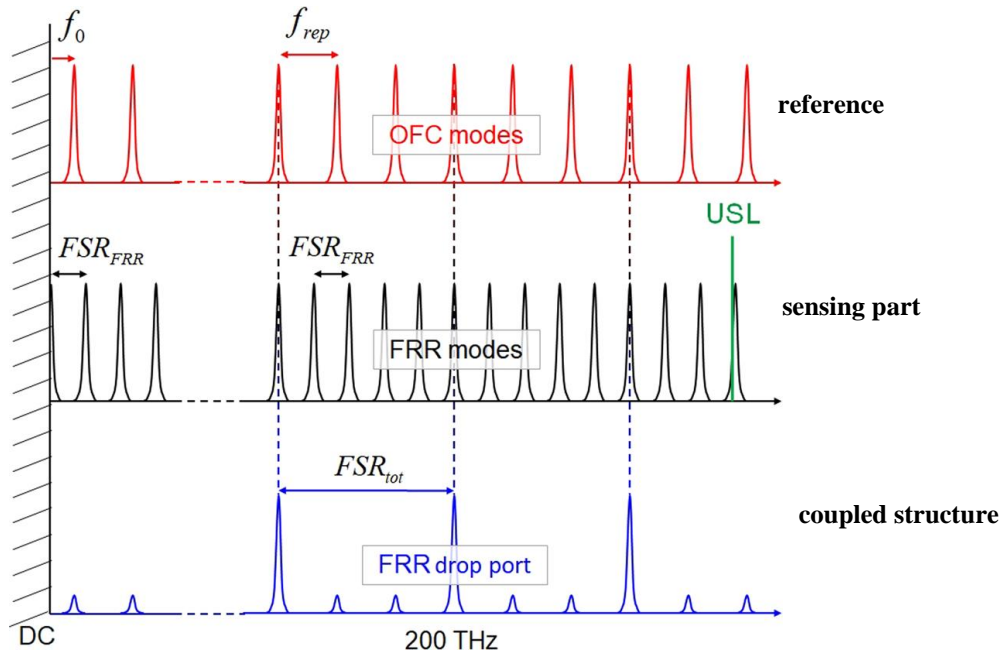
Figure 1.7 Example of the Vernier effect. Optical frequency comb (OFC) is reference part (red). Fibre ring resonator (FRR) is sensing part and generates free spectral range (FSR) (black). While FSRs slide in response to the sensing objets, when FSRs are overlapped with OFC, resonance peaks are filtered (blue). Adapted from [59].

In this thesis, we fabricated a thin corrugated metal structure to excite spoof localized surface plasmons. To easily achieve spoof LSP, we used a commercial inkjet printer with Ag nanoparticles on photopaper. Using these printed samples, we examined whether these samples work or not using monopole source and it was proved that spoof LSP resonances were excited at the printed samples by comparing with the simulation. Although this method is easy, fast and cheap, it has disadvantages in the property of the metal compared to the PCB method. To overcome the limitation of fabrication, we rotated the probes and could clearly observe faint resonances. In addition, we fabricated sensing elements using the 3d printer and obtained elements with a different refractive index. Using them, we conducted sensing test to show the sensing ability of spoof LSP resonators. Lastly, we fabricated not only a single structure but also a coupled one with the Vernier effect. We used two sensing elements for the coupling structure and suggested multiple index sensing concept.

2. Theory

2.1. Surface plasmon

In optical frequency range, metals are described as Drude model, where free electrons in metals are treated as gas moving against positive ions[60]. Dielectric function derived from the Drude model is expressed in equation (1), where ω_p is plasma frequency of the free electron gas and γ is damping constant occurred by collisions [1].

$$\varepsilon(\omega) = 1 - \frac{\omega_p^2}{\omega^2 + i\gamma\omega} \qquad (1)$$

Bound electrons in dielectric material are expressed by the Lorentz model. Permittivity of the materials derived from the Drude or Lorentz model is illustrated in Figure 2.1 (a) [61]. With this information, SPP at flat metal surface can be calculated by solving the Maxwell equation, which confirms that only TM-polarized incident waves can excite SPP. The dispersion relation is expressed as in equation (2), where $k_{||}$ is propagating wavevector along the metal surface, k_0 is wavevector in free space, ε_1 and ε_2 are permittivity of metal and dielectric material.

$$k_{||} = k_0 \sqrt{\frac{\varepsilon_1 \varepsilon_2}{\varepsilon_1 + \varepsilon_2}} \qquad (2)$$

The surface plasmon frequency (ω_{SP}) can be obtained using equations (1) and (2). When $\varepsilon_1 = -\varepsilon_2$, dispersion relation converges to the ω_{SP} which can be expressed like equation (3). Dispersion relation and ω_{SP} are illustrated in Figure 2.1 (b).

$$\omega_{SP} = \frac{\omega_p}{\sqrt{1 + \varepsilon_2}} \qquad (3)$$

There is other kind of SP, which can be excited by a nanoparticle, LSP. LSP frequency (ω_{LSP}) is expressed as (4) and polarizability is important factor. Contrary to SPPs that are largely affected by EM wave polarization and required phase matching, LSP can be coupled with incident light directly because of its additional constraints imposed by finite dimension of nanoparticles [4]. So its dispersion relation is parallel to the x-axis like blue line in Figure 2.1 (b). More detail derivations can be found in [1].

$$\omega_{LSP} = \frac{\omega_p}{\sqrt{1 + 2\varepsilon_2}} \qquad (4)$$

(a)

(b)
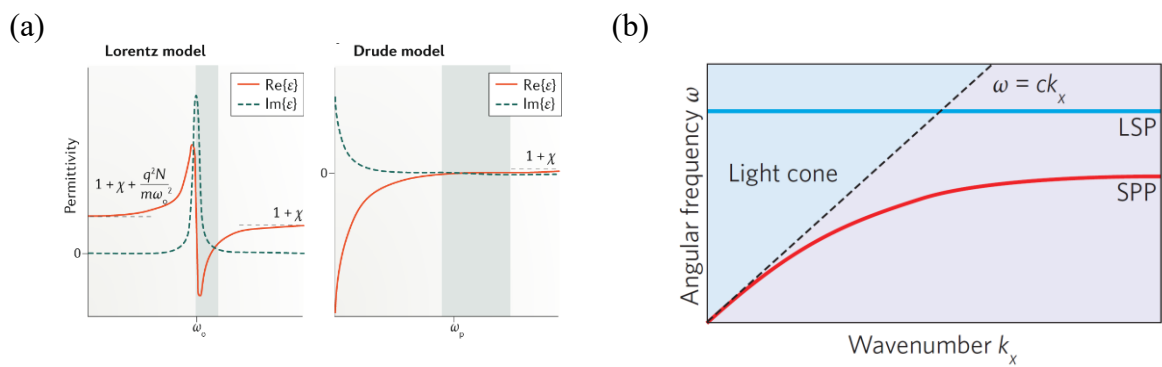
Figure 2.1 Permittivity model and SP dispersion relation at optical frequency region. **(a)** Permittivity graphs as a function of frequency. The Lorentz model (left) and the Durde model (right). Reproduced from [61]. **(b)** Dispersion relation of LSP (blue line) and SPP (red line) in optical frequency region. Light line in free space is denoted as black dotted line. Reproduced from [4].

2.2. Spoof SPP

Spoof plasmon is realized by metal grooves. Pendry et. al [18], first suggested the concept, and the structure is shown in Figure 2.2 (a). They designed a 1D periodically perforated surface structure with PEC metal. To solve the response to the EM waves in this structure, they employed a coupled mode method based on modal expansion and selected p-polarized EM wave(H-field is parallel to the y-axis). The result is represented in equation (5).

$$k_{||} = k_0 \sqrt{1 + \left(\frac{a}{d}\right)^2 tan^2(k_0 h)} \qquad \textbf{(5)}$$

$k_{||}$ is propagating wavevector following the x-axis, k_0 is wavevector in free space, a, d and h are geometric parameters denoted in figure (a). More detail derivation can be found in the [18]. This equation can be also calculated by effective medium approximation, in which surface of the grooves are described by homogeneous and anisotropic material such as blue area in Figure 2.2 (b). In Figure 2.2 (c), the results obtained by the two methods are plotted with $a/d = 0.2$, $h/d = 1$. $k_{||}$ (in units of π/d) and ω (in units of $\pi c_0/2h$) are normalized. The dispersion relation of spoof SPP (Figure 2.2 (c)) is quite similar to the optical SPP (Figure 2.1 (b)) because the graph is converged to asymptote frequency (ω_a) like equation (6),

$$\omega_a = \frac{\pi c}{2h} \qquad \textbf{(6)}$$

which means that the EM wave can be confined near the structure below the ω_a (Figure 2.2 (d)) [25]. So, although the structure is described as PEC, SP can be realized by this grooved metal. It is noteworthy that spoof plasmon is largely affected by geometric parameters a, d, h represented in Figure 2.2(a) and it is confirmed by (5), (6). This result facilitates to change its properties just by modifying structures. On the other hand, there is no parameter related to thickness along the y-axis in these equations because the structure was described as 1D structure. The effect of the thickness in the y-axis has been previously studied, and the results are shown in Figure 2.2 (e) [25]. With decreasing thickness(t), ω_a is decreases while maintaining SP property. Therefore, as in the thin structure, SP can be obtained, which is beneficial in real world for experiment.

(a)

(b) $\varepsilon_x = d/a$ $\varepsilon_y = \varepsilon_z = \infty$ $\mu_x = 1$ $\mu_y = \mu_z = a/d$ h

Perfect conductor

(c)

(d)

(e) Light in free space

t = infinite
t = 20d
t = 2d
t = 0.2d
t = 0.02d
t = 0.002d
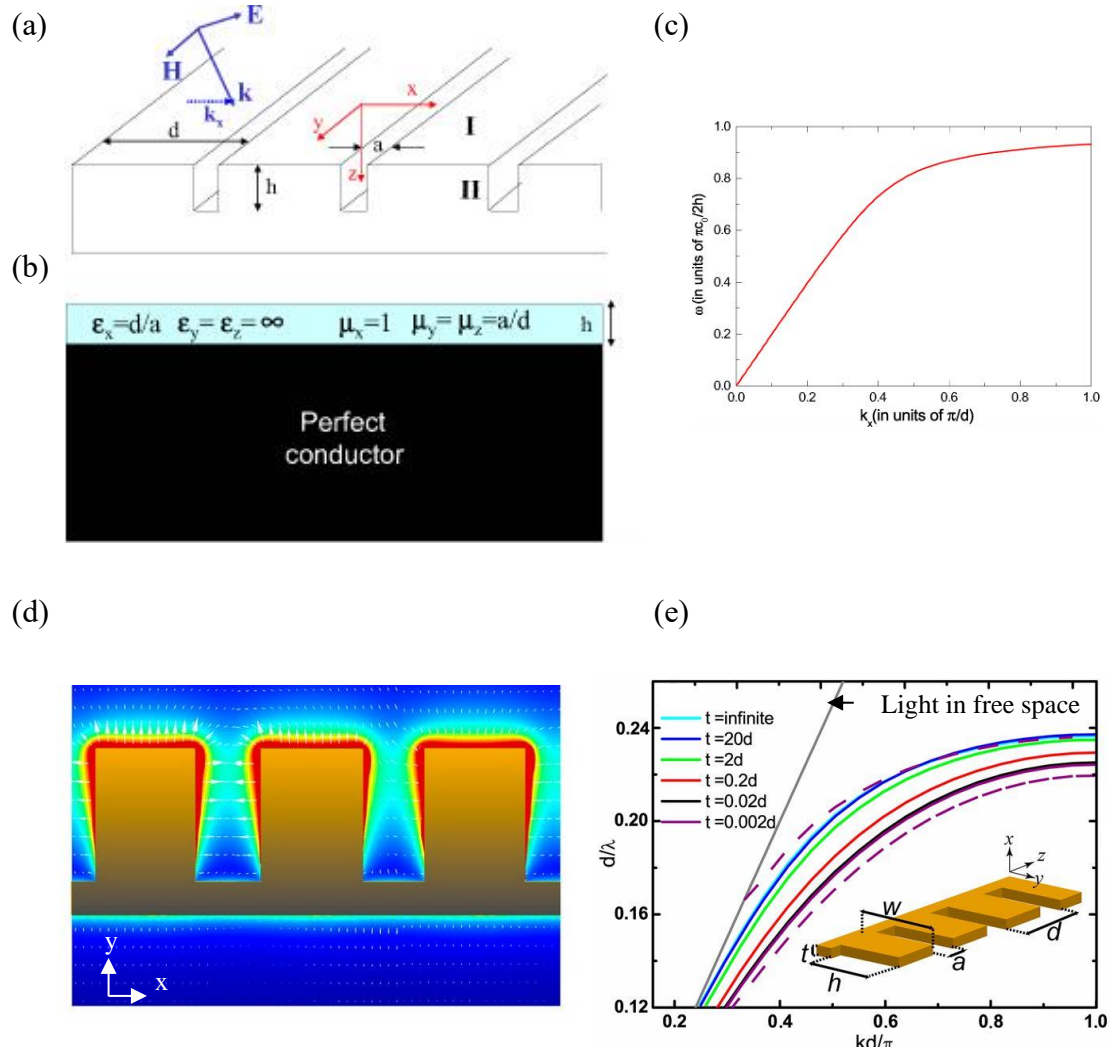
Figure 2.2 Spoof plasmon in 1D grooved structure. **(a)** 1D grooved structure for spoof SPP. EM wave is TM polarization (H-field is parallel to the y-axis). **(b)** Another method to calculate spoof SPP supported by structure in (a); Metamaterial description. **(c)** Dispersion relation obtained by 1D array of grooves such as (a) with a/d = 0.2 and h/d = 1. Reproduced from [19]. **(d)** Field profile near the spoof SPP metal. **(e)** Dispersion relation according to the thickness of the grooved metal. Inset illustration shows the parameters of the thin grooved metal. Adapted from [25].

2.3. Spoof LSP

After several years, spoof LSP concept emerged from same group who suggested spoof SPP [33]. Spoof LSP can be excited in the corrugated metal cylinder like Figure 2.3 (a). Firstly, by the numerical simulation with TM-polarization (H-filed is parallel to the z-axis), the authors showed dispersion relation of the structure is similar to that of optical frequency as in the inset of the Figure 2.3 (c). This result confirms that this structure can excite SP. Also due to the EM wave rotating along structure, the excitation can be regarded as spoof LSP comparable to the nanoparticle in the optical frequency region. In addition, they used the coupled mode method to describe the response of the structure to the EM waves. They used again plane waves propagating toward -y axis with TM-polarization as the simulation. By the boundary condition matching at the dielectric region with $r < \rho < R$ (corresponding to white region within grooves) in Figure 2.3 (a), a transcendental equation was obtained such as (7).

$$S_n^2 \frac{H_n^{(1)}(k_0 R)}{H_n^{(1)'}(k_0 R)} \frac{f}{g} = n_g \tag{7}$$

In this equation, $S_n = \sqrt{a/d}\,\text{sinc}(na/(2R))$ contains all information related to the unit cell and $S_n \approx \sqrt{a/d}$ in the subwavelength unit cell ($a \ll R$); n is mode number (n=1(dipole), 2(quadrupole), 3 (hexapole) modes); $H_n^{(1)}$ is the Hankel function of first kind and order n, k_0 is wavevector in free space; R is larger radius of the structure; f and g are geometry functions represented by Bessel functions; n_g is the refractive index of the dielectric material surrounding the metal. Furthermore, they described the EM response using metamaterial approximation and the illustration is presented at Figure 2.3 (b). Effective parameters are determined like (8) with cylindrical coordinate.

$$E_\rho = E_z = H_\varphi = 0$$

$$\varepsilon_\rho = \varepsilon_z = -\infty \ \text{ and } \ \varepsilon_\varphi = \frac{n_g^2 d}{a} \tag{8}$$

$$\mu_\rho = \mu_z = \frac{a}{d} \ \text{ and } \ \mu_\varphi = \infty$$

Using these parameters, they obtained scattering cross section (SCS) for TM polarized plane wave like as above,

$$\sigma_{SC} = \frac{4c}{\omega} \sum_{n=-\infty}^{\infty} |C_n|^2 \tag{9}$$

, where C_n is the coefficient composed of $H_n^{(1)}(k_0 R)$, f, g and related to SCS of nth azimuthal resonance mode. (A More detailed explanation related to the coupled mode method and metamaterial approximation can be found in [33].) The results are shown in Figure 2.3 (c). At the upper part, complex resonance frequencies obtained from (7) are denoted as black dots and at the bottom, a red dotted line represents the results calculated from (9). In the graph, the two results show that resonance frequencies are quite similar between the two methods and numerical results also correspond to them, proving the

reliability of the two methods. One of the representative properties of the spoof LSP is that multiple resonances exists, such as black dots or peaks of the SCS in Figure 2.3(c). These resonances are occurred by EM wave traveling circularly along the spherical shape. Therefore, when the EM waves satisfy the equation (10), in which *n* is resonance mode in the azimuthal direction and λ is wavelength of the incident light and *$2\pi R$* is perimeter of the structure, resonances are excited as a form of standing waves. It is confirmed by Figure 2.3 (d). There are H-magnitude field profiles extracted from resonance peaks in Figure 2.3 (c) black line and the profiles correspond to hexapole, octupole, decapole resonances. As a result, by exciting spoof LSP, we can observe multiple resonances in the corrugated metal cylinder.

$$n\lambda = 2\pi R \ (n = 1,2,3,\cdots) \qquad\qquad \textbf{(10)}$$
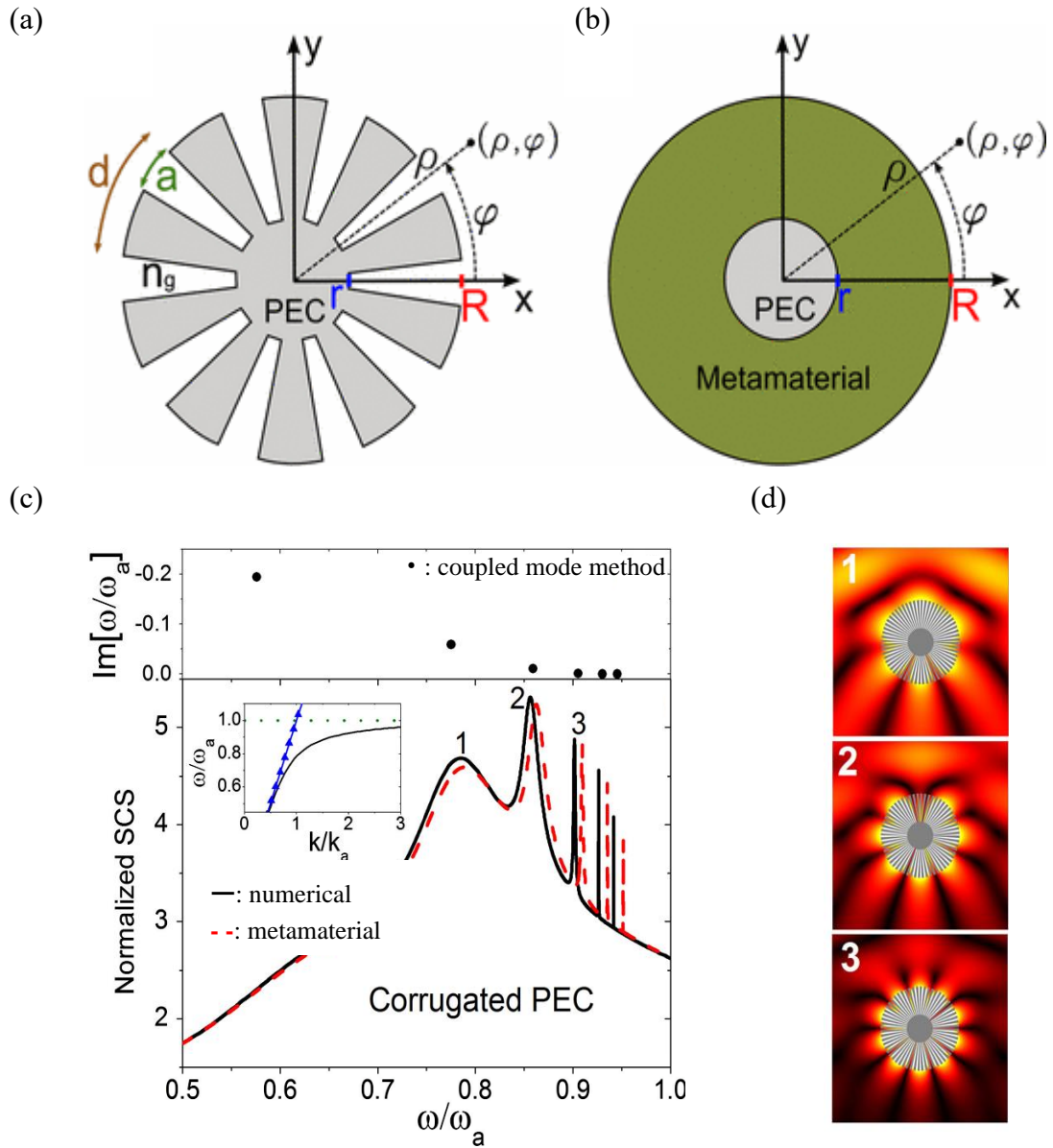
Figure 2.3 Illustrations of spoof LSP structure and results. **(a)** Illustration of grooved 2D cylinder to describe spoof LSP structure. **(b)** Illustration of effective medium approximation for the structure in (a). **(c)** Results of spoof LSP calculated by modal expansion technique (black dots in above figure), metamaterial approximation (red dotted line) and numerical calculation (black line). **(d)** Field profiles of |H| component. The marked numebers in each field profile correspond to the number denoted on resonance peaks in (c). Adapted from [33]

Meanwhile, Z. Liao et. al. calculated dispersion relation of the spoof LSP using Mie scattering and an effective medium approach [46]. They obtained SCS equation that is similar to (9). By taking the limit k_0R, $k_0r \gg 1$, they achieved dispersion relation and the result is represented in equation (11),

$$\frac{n}{R} = k_0 \sqrt{1 + \left(\frac{a}{d}\right)^2 tan^2(k_0 h)} \qquad \textbf{(11)}$$

In this equation, $n/R = 2\pi/\lambda = k_\parallel$ from (10), so the right side of (11) correspond to propagating wavevector, $k_\parallel$. Actually, this equation is the same as the spoof SPP dispersion relation, as in (5). It can be explained by making the unit cell of 2D cylinder as radial grooves or parallel walls such as Figure 2.4 [34]. N number of the unit cells form 2D corrugated cylinders. At first, cylinder is treated with radial groove units like figure (a). In the figure, gray is PEC metal and green is dielectric index. Assuming that dielectric is filled with air, as in figure (a), the cylinders with radial grooves can be described by equation (7) through modal expansion. On the other hand, with unit cells of parallel walls like figure (b), the equation of the structure is expressed by equation (12),

$$S_n^2 \frac{H_n^{(1)}(k_0 R)}{H_n^{(1)'}(k_0 R)} \tan(k_0 n_g h) = n_g \qquad \textbf{(12)}$$

, where

$$S_n = \sqrt{\frac{a}{d}} \, \text{sinc}\left(\frac{n\pi a}{Nd}\right). \qquad \textbf{(13)}$$

In this case, to compensate for the circular shape, Born von Karman boundary condition was applied for a super-cell whose length is $\Lambda = 2\pi R$. So the overlap integral of the equation (13) gives it the same equation as S_n in equation (7). Moreover, the asymptote frequency of the spoof LSP can be calculated by (14),

$$\omega_a = \frac{\pi c}{2h n_g} \qquad \textbf{(14)}$$

, similar to spoof SPP asymptote equation (6) except for refractive index filling the grooves (n_g). Consequently, the same dispersion relation between spoof SPP and LSP is proved and spoof LSP can be realized by bending the flat metal grooves of the spoof SP structure.

1 7
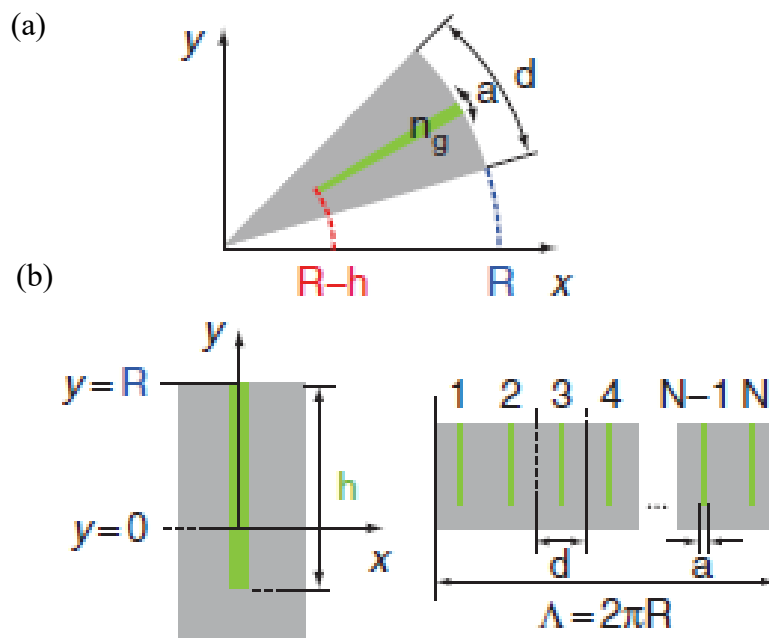
Figure 2.4 Unit cells to derive spoof LSP by modal expansion technique within **(a)** radial grooves and **(b)** parallel walls structure. Gray denotes PEC metal and green dielectric material with n_g. Reproduced from [34].

3. Results and Discussion

So far, spoof plasmon is explained. From now on, we will show what we have studied exploiting the spoof LSP. To realize the spoof LSP easily, we used inkjet printer. Printed samples were measured and the results were compared to the simulations. By rotating the probes to be located at unconventional positions, we observed interesting results. In addition, there are many efforts to study the dielectric sensing so we will show its sensing ability using refractive index sensing elements fabricated by a 3d printer. Lastly, we used not only the single structure but also coupled structure with Vernier effect. We selected one dominant peak and introduced one concept to realize multiple index sensing or complex signals.

3.1. Sample fabrication (Inkjet printing) and measurement

To conveniently realize spoof plasmon, we used common inkjet print, illustrated in Figure 3.1. Firstly, we designed structures of the samples. Using EPSON STYLUS C88 plus, we then filled inkjet cartridge with liquid silver nanoparticle ink. Finally, we annealed the printed samples using an oven set to 180℃ for 3 minutes. We selected photo-pater as a substrate because of its porosity, which helps the ink to penetrate into the paper via capillaries. Although this method is worse than the lithography or PCB method, in view of the fabrication process, it is easier, cheaper, faster and consumes less material.
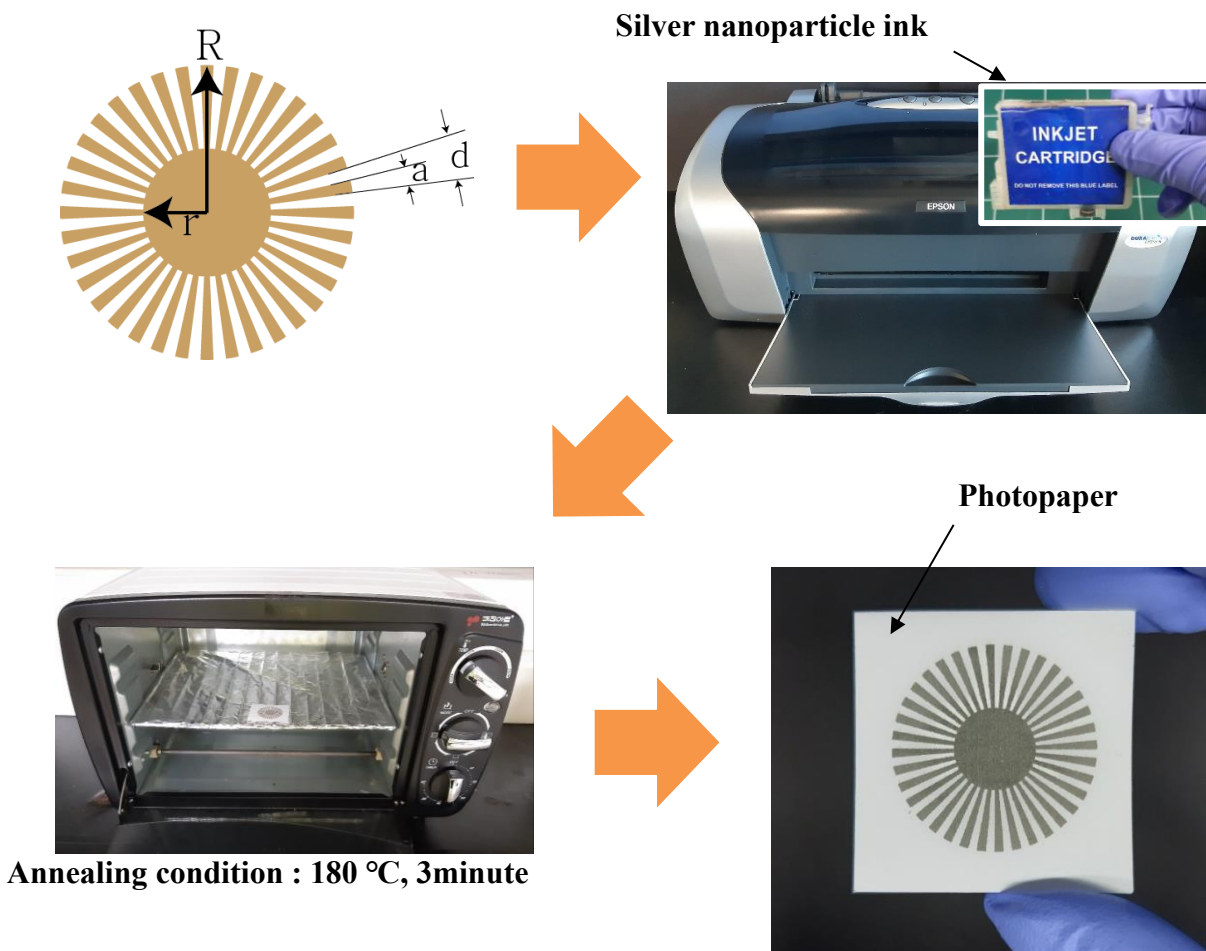
Figure 3.1 Procedure to fabricate spoof LSP resonators; (1) design the structure; (2) facilitate inkjet printer (EPSON STYLUS C88) with silver nanoparticle on paper; (3) conduct annealing at 180℃ for 3 minutes. Last picture is a final sample**.**

To identify the quality of the printed samples, we obtained SEM images. Before annealing, the size of the nanoparticles must be less than 100nm (Figure 3.2 (a)). By increasing annealing temperature, the particles grow (Figure 3.2 (b) and (c), corresponding to 120℃ and 150℃, respectively). Finally, when annealing temperature approaches 180℃, lots of nanoparticles are larger than 200nm (Figure 3.2 (d)), which are conducive to make conductive channel. However, if the temperature and time exceeds 3 minutes and 180℃ (Figure 3.2 (e)), although the size of nanoparticle is larger, the samples started to burn, as in Figure 3.2 (g). This burning also happens under temperatures larger than 180℃. So we determined the annealing condition to be 180℃ for 3 minutes. Completed annealing samples are represented in Figure 3.2 (f). The conductivity of annealing processed samples is $2.5 \times 10^6 \ \Omega^{-1} m^{-1}$.

(a)

Before Annealing

83.0nm

74.0nm

71.0nm

67.0nm

86.0nm

UNIST 10.0kV 7.9mm x50.0k SE(U)   1.00μm

(b)

120℃, 3 min

115nm

119nm

138nm

112nm

UNIST 10.0kV 7.8mm x50.0k SE(U)   1.00μm

(c)

150℃, 3 min

155nm

149nm

169nm

146nm

136nm

UNIST 10.0kV 7.7mm x50.0k SE(U)   1.00μm

(d)

180℃, 3 min

142nm

270nm

235nm

133nm

201nm

UNIST 10.0kV 7.6mm x50.0k SE(U)   1.00μm

(e)

180℃, 10 min

204nm

211nm

192nm

161nm

257nm

181nm

UNIST 10.0kV 7.7mm x50.0k SE(U)   1.00μm

(f)

180℃, 3 min

(g)

180℃, 10 min

Figure 3.2 SEM images according to different annealing condition. **(a)** Before annealing process. **(b)** At 120 ℃ for 3 minute. **(c)** At 150 ℃ for 3 minutes. **(d)** At 180℃ for 3 minutes. **(e)** At 180 ℃ for 10 minute. All the scale bar denotes 1μm. **(f)** is a picture of final sample for annealing condition (d). **(g)** is annealing condition for (e)

3.2. How to measure and simulate Spoof LSP

Printed samples are excited by a monopole antenna and measured by Vector Network Analysis (VNA). One end of a coaxial cable is connected with VNA and the other with SMA for impedance matching. We used 2 monopole antennas for the transmission of the samples. The S1 port acts as a source and S2 as detector and we measured S21 value. After electric calibration, we started measurements from 1 to 15GHz range. Figure 3.3 (a) represents the measurement set-up.

To verify the measurement, we conducted a finite-difference-time-domain (FDTD) simulation. We located the two probes horizontally to the metal at the same plane, 1mm apart from the metal. For the boundary condition, we used a perfectly matched layer (PML), as shown in Figure 3.3 (b). It is noted that although metal can be treated as a PEC at a few GHz, we used finite conductivity. As previously mentioned, our fabrication method has tradeoff between property and fabrication advantage so our inkjet printed samples showed little conductivity, 2.5×10^6 $\Omega^{-1}m^{-1}$, with thickness about 1μm. Thus, we adopted this conductivity value to the metal in simulation. Furthermore, the photopaper is much thinner than EM wavelength, which can be ignored. Except for little resonance differences between measurements and simulations, the results are quite similar. So simulation without substrate can be acceptable.

(a)

VNA (Vector Network Analysis)

S1(source) S2(detector)

Coaxial cable

SMA

(b)

PML (perfectly Matched Layer)
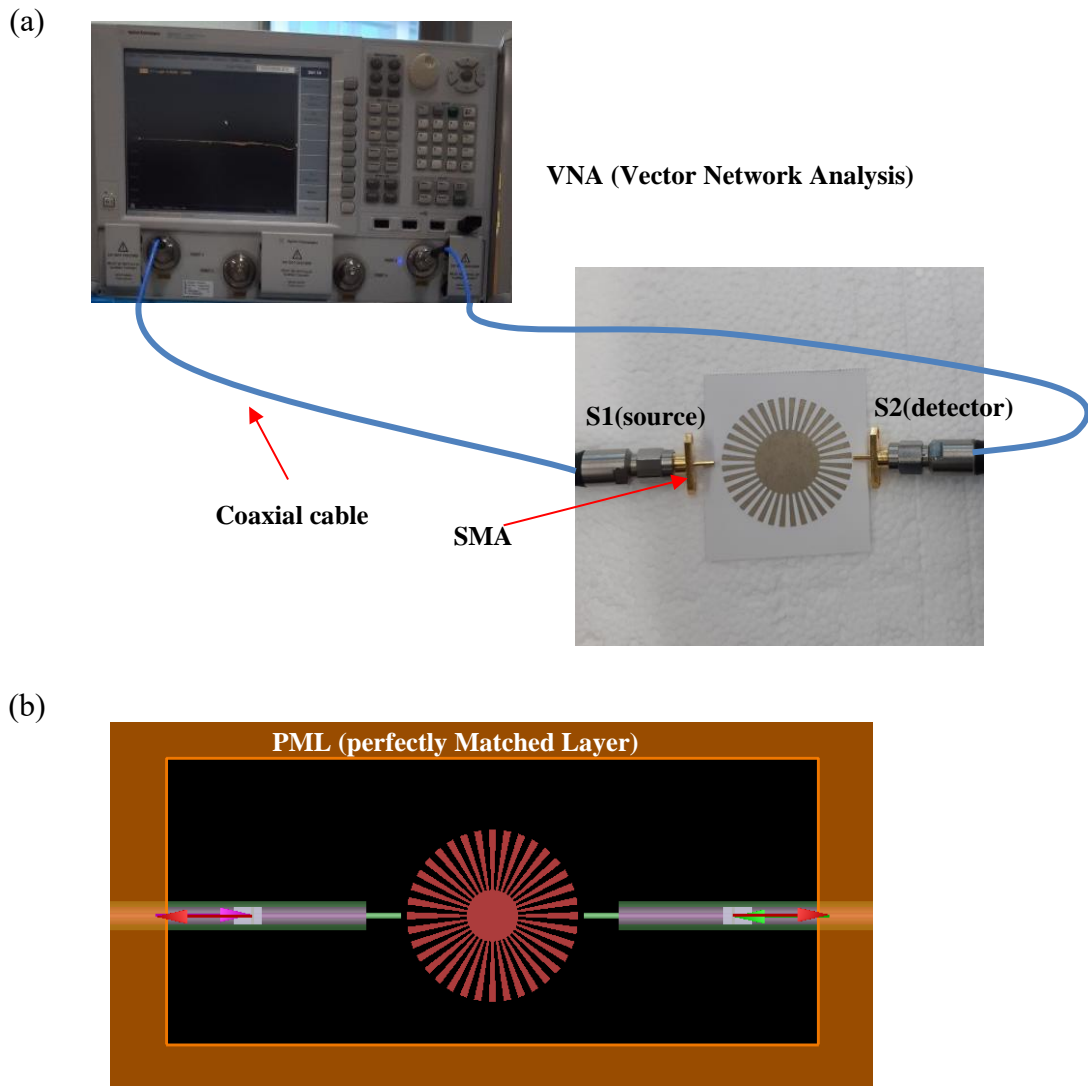
Figure 3.3 Measurement set-up and simulation display. **(a)** Vector analysis network (VNA) is connected with SMA, S1 port (source) and S2 port (detector). Samples are measured like right picture. **(b)** Captured FDTD simulation display. Left probe is S1 port and right is S2 port. Metal is not PEC metal but 2d conductive material with conductivity = $2.5×10^6$ $\Omega^{-1}m^{-1}$ and thickness = 1μm. All the sides are surrounded by perfectly matched layer (PML).

3.3. Spoof LSP dispersion relation

Before measurement, we simulated and calculated dispersion relation to better comprehend properties of spoof plasmon. We designed spoof LSP resonators like those in Figure 3.4 (a), while fixing $R = 15$mm and changing r from 3mm to 12mm with $\Delta r = 1$mm. Figure 3.4 (b) illustrates how probes were situated during simulation. We calculated the dispersion relation of the designed samples using equation (11). As shown in dispersion relation, Figure 3.4 (c), increasing r results in higher asymptote frequency which can be explained by equation (14). In the equation, $h = R - r$. So, h decreases in negative proportion to r, which increases ω_a. This result causes resonance peaks to shift to higher frequency in the simulation for $|S_{21}|$ value (Figure 3.4 (d), easy to see, we adjusted the values along y-axis). In addition, we can observe resonance peaks for each r in the simulation, which is representative properties of spoof LSP as previously noted. But the number of the resonance peaks we find clearly is different according to the r. In larger r, more resonances appear. Because the slope of the dispersion relation is gradually decreased with increasing r, $k_{\parallel}$ values slowly change with increasing frequency. So much more and higher resonance modes can be excited at larger r. This finding is supported by field profiles. We selected two structures whose $r = 4$mm or 11mm and Figure 3.4 (e) and (f) correspond respectively to each structure. The fields are E_z component at 0.5mm above the metal. The numbers below the field profiles correspond to frequency point denoted in Figure 3.4 (d). From the field profiles, when $r = 4$mm (Figure 3.4 (e)) , only quadrupole (i) and hexapole (ii) resonances can be observed. On the other hand, when $r = 11$mm(Figure 3.4 (f)), octupole (iii), decapole (iv) and more higher modes(v, vi) are represented.
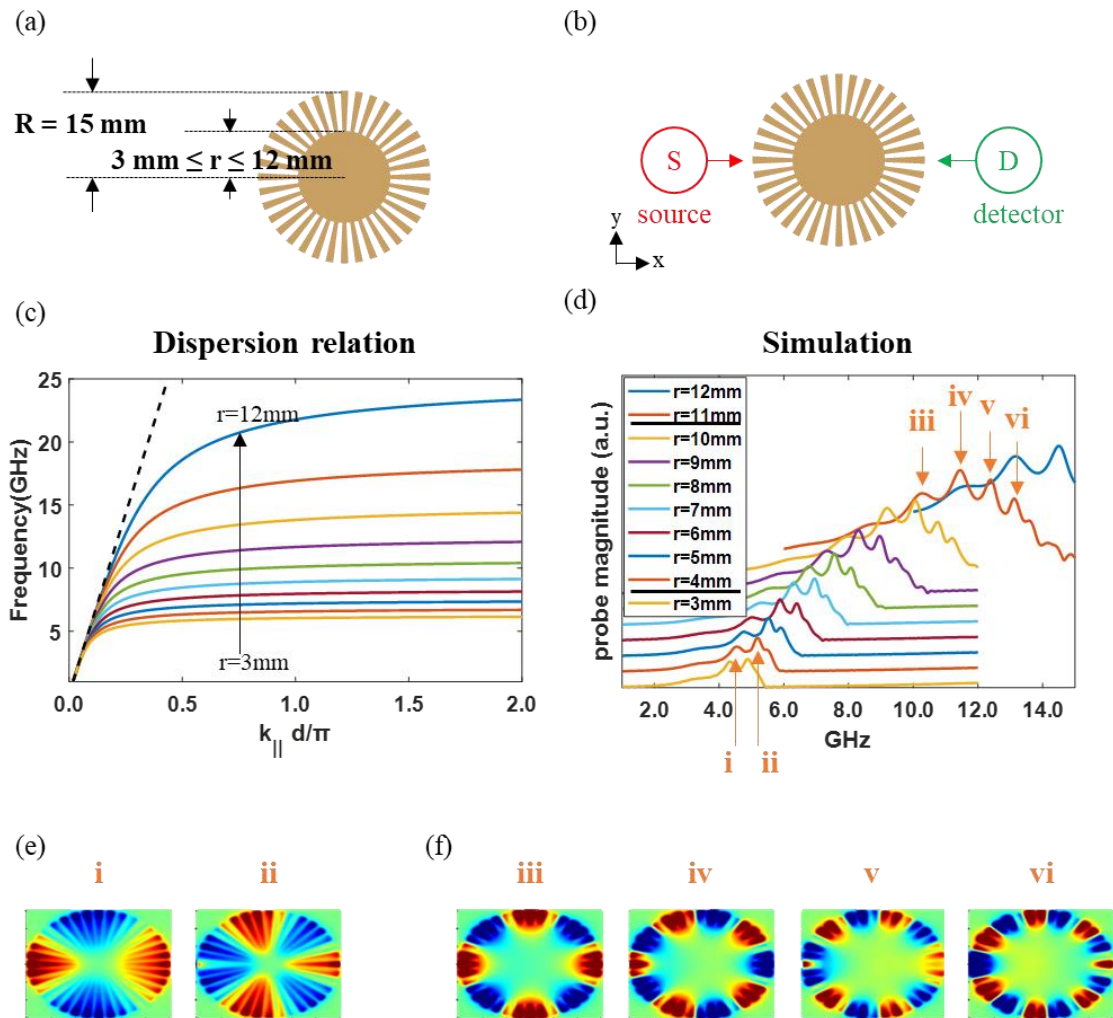
Figure 3.4 Dispersion relationa and simulation results for designed spoof LSP structures. **(a)** Designed resonators. Large radius, R, is fixed as 15mm but small radius, r, is changed from 3mm to 12mm with $\Delta r = 1$mm. **(b)** Simulation condition. Source and detector are arranged in parallel. **(c)** Dispersion relation for designed structures. $k_\parallel$ is normalized by d/π. **(d)** Simulation results for |S21| value. Easy to see, we adjusted the values and separated along y-axis direction. **(e)**, **(f)** are field profiles for $r = 4$mm $r = 11$mm, respectively. The numbers on the file profiles correspond to resonance peak in (d).

3.4. Probe rotation

Selecting one of the structures in the above section, $R = 15$mm and $r = 4.5$mm, we measured |S21| value. At first, we measured the sample by locating the probes facing each other. In Figure 3.5 (a), the situation is described and S(D) with red(green) color denotes S1(S2) port, in other word source(detector). Results are represented as blue curve denoted as **S1 0°** in simulation (Figure 3.5 (c)) and measurement (Figure 3.5 (d)). As we see these graphs, simulation and measurement results are quite coincident with each other. One thing to note is that resonance in measurements are slightly red shifted compared to the simulation. As I mentioned above, because the substrate is thin enough compared to the wavelengths of the measured frequencies, we didn't apply a substrate in the simulation. Except for this small red shifts, all the results look quite similar. Therefore, it was proved that the printed samples worked well. In the graphs, there are three resonance peaks and each one corresponds to quadrupole, hexapole and octupole as denoted in the graphs. However, although we can observe octupole peak in the simulation, we cannot in measurement due to the limitation of the fabrication by metal inkjet printing.

To overcome it, we tried a trick. By rotating the **S1 90°** counterclockwise, as in Figure 3.5 (b), we converted the hexapole peak into dip. The results are represented as an orange curve in both Figure 3.5 (c) and (d). We denoted the conversion in the graphs using black arrows. In this way, faint octupole resonances become clear both in simulation and measurement. This can be explained by field profiles which captured E_z field at 0.5mm above the metal as before. Figure 3.5 (e) corresponds to the (a) situation. Each field profile originates from hexapole and octupole resonance peaks of blue curve in the simulation. In this case, the detectors are located at the field maxima both in hexapole and octupole resonances. So the blue curve shows only resonance peaks. Otherwise, in Figure 3.5 (f), which corresponds to the (b) situation and orange curve in the graphs, rotating the source counterclockwise 90° lets the detector be located at the field node of the hexapole resonance. So the measured transmission value of the hexapole resonance is very low, which results in resonance dip in the orange graph. However, in the octupole resonance, the detector is still located at field maxima, so S_{21} value still appears as a resonance peak. Using this trick, we converted the resonance peak into a dip enabling us to use more resonances.
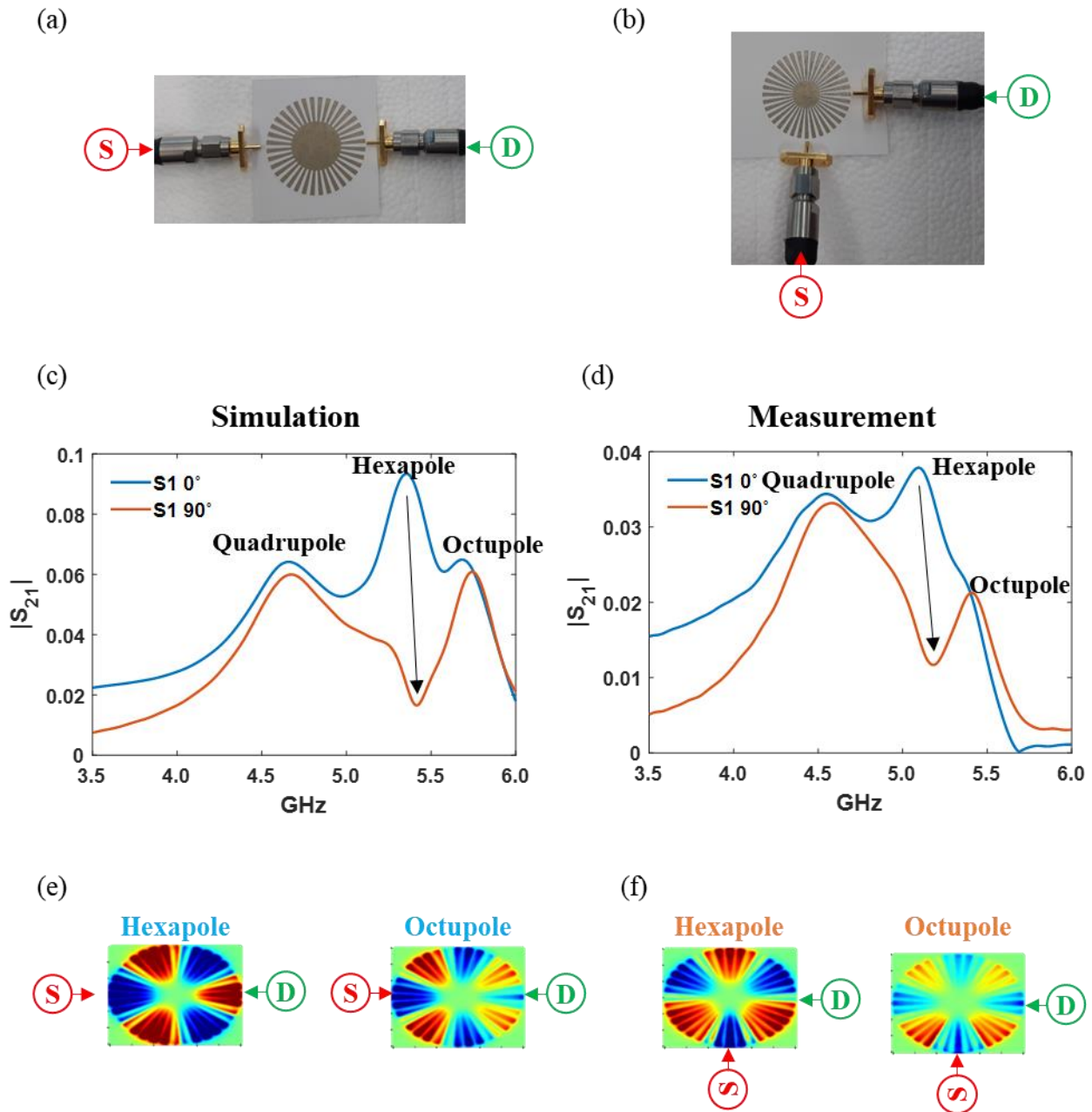
Figure 3.5 Probe rotation measurement. **(a)** Probes are placed facing each other or **(b)** orthogonally. **(c)** Simulation results. **(d)** Measurement. In the simulation and measurement, (a) case is represented as blue curve (*S1 0˚*) and (b) as orange curve (*S1 90˚*). **(e)** Field profiles from simulation for *S1 0˚* case correspond to the hexapole and octupole resonance peaks. **(f)** Field profiles for *S1 90˚* case correspond to the hexapole resonance dip and octupole resonance peak. Fields profile represent Ez component captured above 0.5mm from metal.

2 8

3.5. Index sensing test

To test sensing ability in spoof LSP, we fabricated sensing elements by 3D printing, as in Figure 3.6. Material used for 3D printing is Vero White with refractive index = 1.6. The radius of printed sensing elements is 5mm, less than wavelength of measurement frequency (λ = 30mm at 10GHz). Therefore, the refractive index can be calculated by effective medium method, as in equation (15).

$$n = 1 \times (1 - f.f.) + 1.6 \times f.f. \qquad \textbf{(15)}$$

In this equation, n is the refractive index of the sensing element. 1 and 1.6 originate from the refractive index of air and Vero White. By adjusting the fill factor (*f.f.*, from 0 to 1) of the samples, we achieved a refractive index value between from 1 to 1.6. Figure 3.6 shows the printed sensing elements. With increasing *f.f.*, refractive index *n* increased. We selected *f.f.* = 0.2, 0.4, 0.6, 0.8, 1 and refractive indexes(*n*) correspond to 1.12, 1.24, 1.36, 1.48, 1.6.
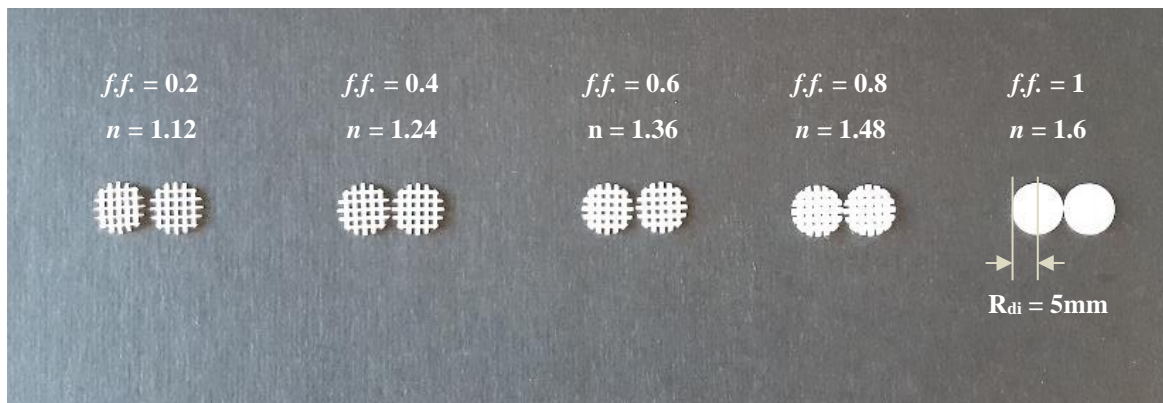
Figure 3.6 Sensing elements fabricated by 3d printing. Radius of the elements are 5mm By adjusting fill factor (*f.f.*) of the elements, we obtained *f.f.* = 0.2, 0.4, 0.6, 0.8, 1 and they correspond to refractive index (*n*) = 1.12, 1.24, 1.36, 1.48, 1.6.

Using these sensing elements, we conducted a sensing test for the spoof LSP resonator, which is used in Section 3.3 (R = 15mm, r = 4.5mm). Firstly, we simply put one dielectric element on the edge as in the inset of Figure 3.7 (a), which is similar to Figure 3.5 (a), while changing the sensing element. We denoted resonance peaks in the Figure 3.7 (a) and each peak corresponds to quadrupole, hexapole and octupole from lower to higher frequency sequentially. Increasing fill-factor, in other words, increasing index red-shifts the resonance peaks and decreases $|S_{21}|$ intensity in simulation. These trends are commonly observed in other articles [38, 48, 51, 62]. And measurements in Figure 3.7 (b) are matched well to simulations. We analyzed hexapole resonance peaks, shown as Figure 3.7 (c) and (d). In these graphs, black(red) lines indicate frequency($|S_{21}|$ intensity) of the peaks and value is represented at the left(right) y-axis. As previously mentioned, resonance frequencies are red-shifted and intensities are reduced in the analysis graph with increasing index or fill-factor. Likewise, by establishing the amount of frequency shift and S_{21} intensity variation according to refractive index, we can apply spoof LSP resonators to the refractive index sensors such as other resonators [63, 64].
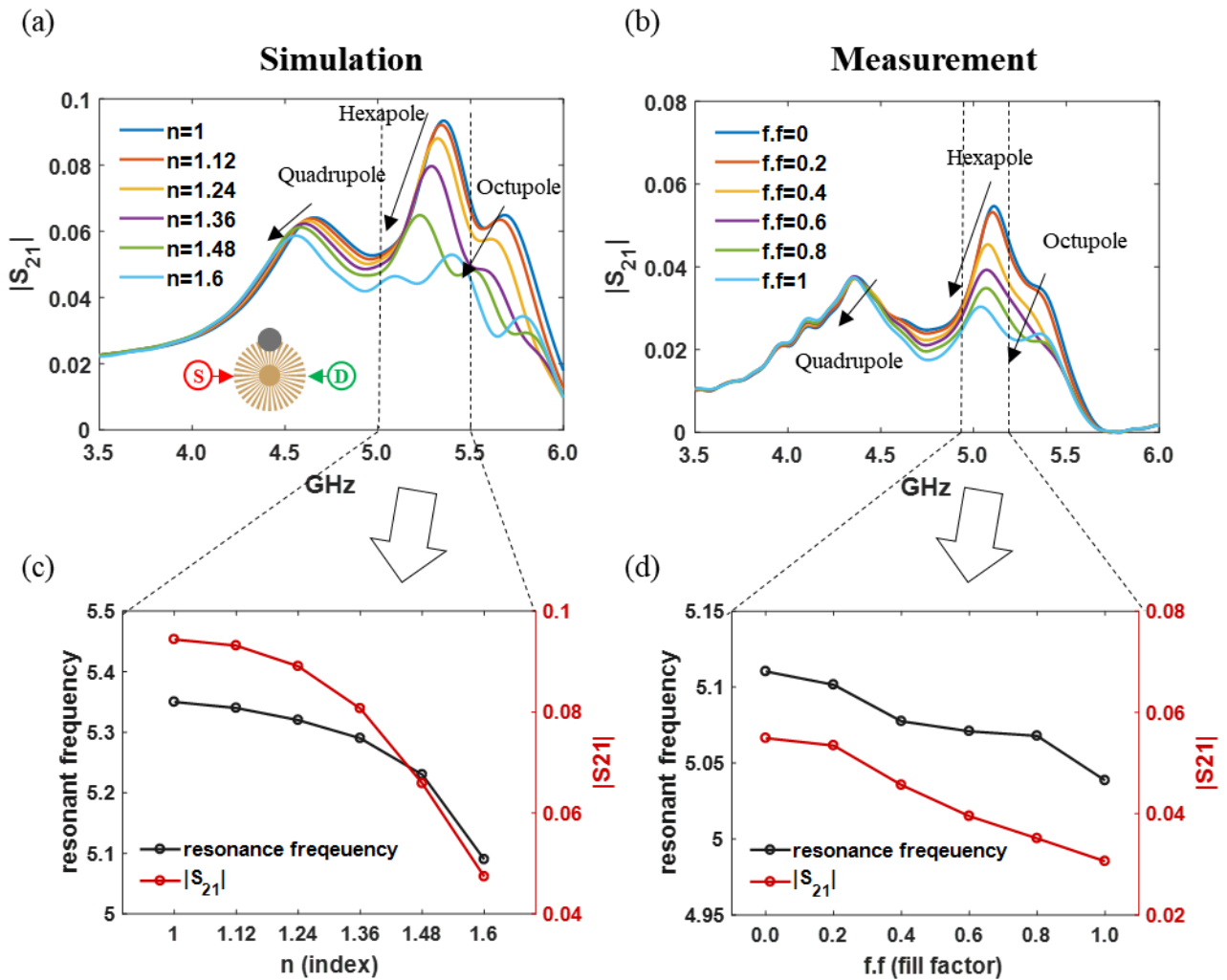
Figure 3.7 Index sensing test with probe arrangement in horizontal. **(a)** Simulation results. Inset of the figure represents probe arrangement. **(b)** Measurement results. In (a) and (b), three resonance peaks correspond to the quadrupole, hexapole and octupole resonances. Black arrow lines show resonance peak shifts according to the increasing refractive index in simulation and the increasing fill factor in measurement. **(c)** Analysis of the hexapole resonance peaks in simulation (a). **(d)** Analysis of the hexapole resonance peaks in measurement (b). Left y-axis with black color represents resonance frequency and right y-axis with red color |S21|.

For another case, we located source and detector orthogonally, as in the inset of Figure 3.8 (a). It is similar to Figure 3.5 (b) and we again used the same resonator (R = 15mm, $r = 4.5mm$). Due to the probe being rotated counterclockwise 90˚, hexapole resonances emerge as dips in the results. From the simulation results Figure 3.8 (a), we can observe all the resonances are red-shifted with increasing *f.f.* or refractive index. However, $|S_{21}|$ intensities of hexapole dips increase opposite to the quadrupole or octupole resonance peaks, which are decreased. We analyzed this result in detail in Figure 3.8 (c). We see that although the hexapole resonance frequencies are reduced following the increasing refractive index, intensities increase. Actually, resonances are getting weaker according to increasing dielectric index. So, unlike resonance peaks where S_{21} intensities decreases proportionally to the larger refractive index, the week resonances are expressed as an increased $|S_{21}|$ intensities at this hexapole resonance dips. In addition, it is noted that octupole resonance become clarified compared to the Figure 3.7 in which the octupole resonance is faint, so one more resonance can be used for refractive index sensing. Furthermore, except n = 1.6, frequency shifts of hexapole resonance dips in Figure 3.8 (c) are larger than hexapole peaks Figure 3.7 (c). This indicates that deploying source and detector orthogonally makes the resonances more sensitive for refractive index variation compared to the parallel deployment. Although frequencies of these dips are well matched between simulation and measurement, S_{21} values are not. In measurement, these hexapole dips are obscure. This discrepancy can be corrected by elaborate measurement.
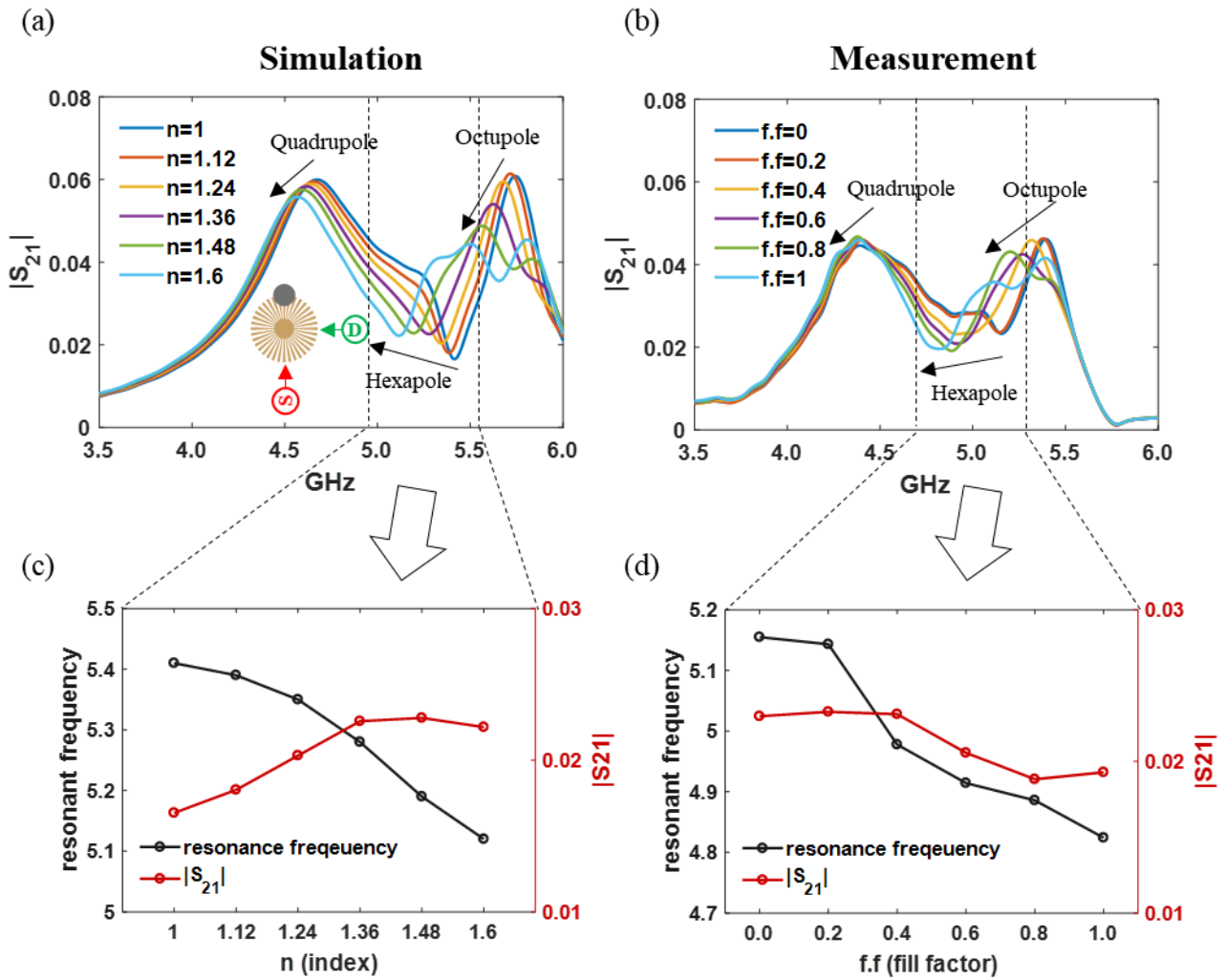
Figure 3.8 Index sensing test with probe arrangement in orthogonal. **(a)** Simulation results. Inset of the figure represents probe arrangement. **(b)** Measurement results. In (a) and (b), two resonance peaks correspond to the quadrupole, octupole and one resonance dip to hexapole. Black arrow lines show resonance peak shifts according to the increasing refractive index in simulation and *f.f.* in measurement. **(c)** Analysis of the hexapole resonance dips in simulation (a). **(d)** Analysis of the hexapole resonance dips in measurement (b). In (c) and (d), left y-axis with black color represents resonance frequency and right y-axis with red color |S21|.

3.6. Coupled structure with Vernier effect

There are many studies related to coupling between spoof LSP resonators [41-43, 45, 65, 66]. We used the coupled structure for the multiple sensing test. In addition, we adopted the Vernier effect which is widely used for sensing in optical frequency [56-59]. The Vernier effect is coupling of two resonators, between the reference and sensing parts. As in Figure 1.7, the two resonators have periodic resonances in the shape of a comb. While resonances of reference parts are not shifted, sensing parts slide to the lower frequency in response to the sensing material. During sliding, if the resonances in sensing part match with the reference's one, the overlapped peaks are filtered. Actually, resonances of our samples are not quite sharp because of the fabrication limitation, so filtering the resonances would be helpful for the sensing experiment.

For the resonance filtering, we designed two single resonators. For the larger one, $R_1 = 18$mm, $r_1 = 10.8$mm; for the smaller one is $R_2 = 15$mm, $r_2 = 8.25$mm. Simulation results of these two resonators are shown in Figure 3.9 (a), where the larger one is denoted as a blue curve, and the smaller one as an orange one. To achieve $|S_{21}|$ value, we set the probes facing each other like inset of Figure 3.9 (c) and (d). In the simulation results, resonance peaks of each structure are overlapped near 7GHz denoted as f_2 with a solid arrow line in the graph and the resonances correspond to hexapole and octupole for smaller and larger resonator, respectively, supported by field profiles in Figure 3.9 (c) and (d). By combining the two resonators with gap = 10mm between them, we obtained a coupled structure. We simulated the coupled structure with probes facing each other, as inset of Figure 3.9 (e) and the results are shown as the yellow curve. Except one intended peak at f_2, other peaks are filtered and the simulation results correspond to the measurement, also denoted as a yellow graph in Figure 3.9 (b). As mentioned above, due to the absence of substrate in the simulation, there are slight red shifts of resonance peaks in measurement compared to the simulation. Nevertheless, we can find the filtered f_2 resonance peak in the measurement (Figure 3.9 (b)).

However, due to the large scattering at lower-order resonance, the unwanted peak denoted as f_1 with a dashed black arrow line still exists. It arises from hexapole resonance of the larger resonator verified by the left field profile in Figure 3.9 (c). To suppress this unwanted peak, we again tried the trick, in which probes are rotated as the illustration in Figure 3.9 (f). The source (S_1 port) and detector (S_2 port) are rotated 22.5°, 90° counterclockwise, respectively. The result is represented as a purple curve. Finally, we made only one overlapped peak (at f_2) alive while the unwanted peak (at f_1) suppressed both in the simulation and measurement. This result can be explained by field-profiles. In Figure 3.9 (e) and (f), left ones are field profiles at f_1, where unwanted peak exists, and right ones are at f_2, as intended. Before rotating them, the detector is located at field maxima for both f_1 and f_2, as in Figure 3.9 (e). On the other hand, rotating the probes like Figure 3.9 (f) leads fields to be rotated following the source. The position of the source corresponds to field maxima in the field profiles. So it is observed that the field of left

resonators are rotated at both f_1 and f_2., compared to the Figure 3.9 (e). The rotated field of the left one then induces the right one to also rotate. At f_1, the detector is located at a field node, although the detector is still located at field maxima in f_2. Consequently, in the (f) case the unwanted peak at f_1 is suppressed and the overlapped peak at f_2 persists. In addition, it is confirmed that the simulation results agree well with the measurement.
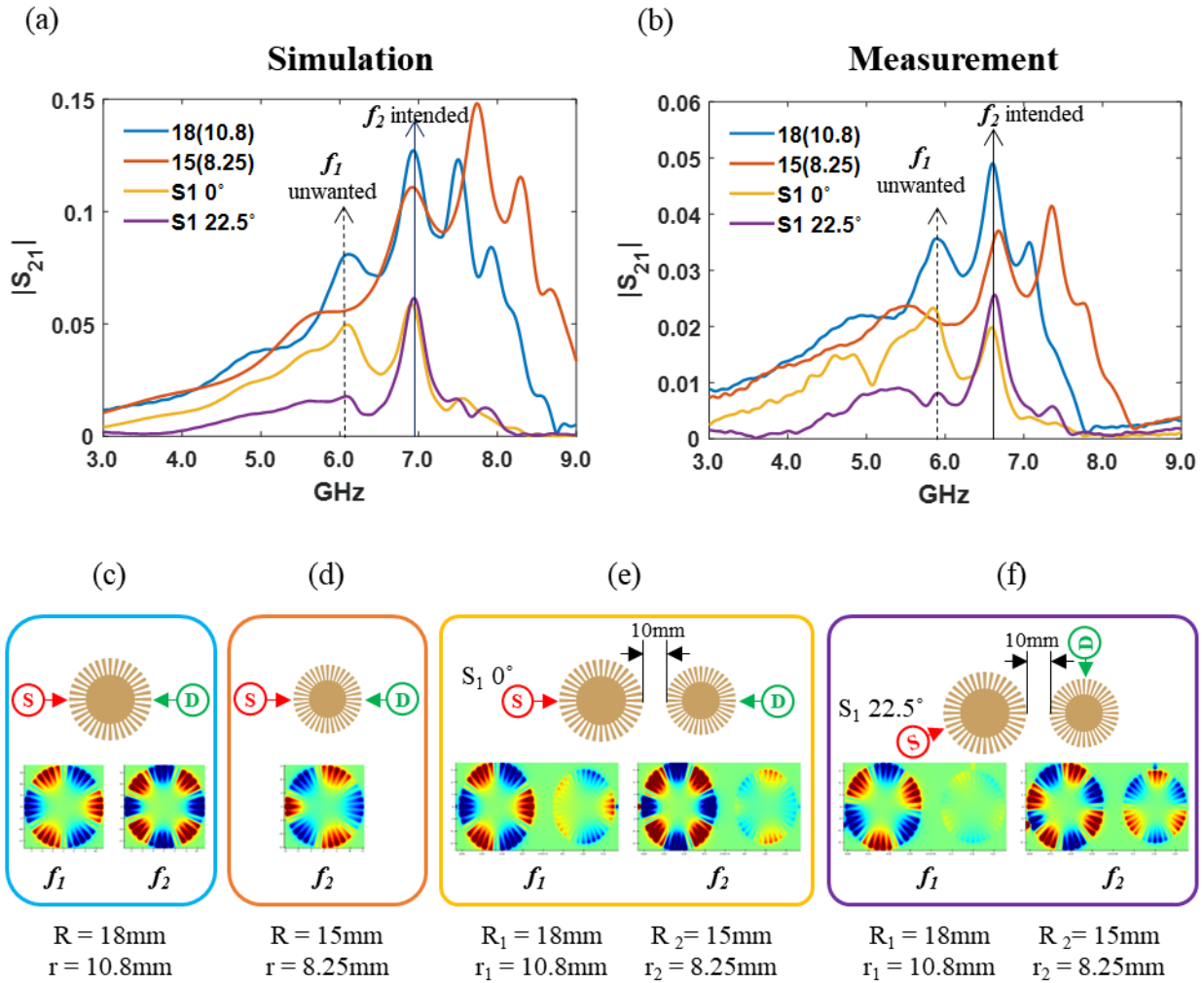
Figure 3.9 Coupled structure with the Vernier effect. **(a)** Simulation result. **(b)** Measurement. In (a) and (b), blue, orange lines correspond to the larger (R = 18mm, r = 10.8mm) and smaller resonator (R = 15mm, r = 8.25mm). Yellow line is the results of coupled structure by setting the probe facing each other (S1 0°) such as inset of (e) and purple line is the results of coupled structure with rotated probes (S1 = 22.5° and S2 = 90° in counterclockwise) such as inset of (f). The coupled structure is a combination of larger and smaller resonators. In (a) and (b), we denoted unwanted frequency (f_1) with doted line and intended frequency (f_2) with solid line. Especially at f_2, hexapole resonance from smaller resonator and octupole resonance from larger resonator are overlapped. **(c)** and **(d)** are field profile of larger and smaller resonator. **(e)** and **(f)** are field profiles of coupled structure with different probe location like inset of them. Field profiles come from f_1 and f_2 as indicated below them.

Through the aforementioned trick, we realized resonance filtering motivated by the Vernier effect. Actually, this overlapped peak will respond sensitively to the shift of each single resonator. Therefore, as Vernier effect has usually been applied to the sensors, we conducted a sensing test using the coupled structure.

For the sensing test, we slightly reduced the radius of the larger resonators from $R_1 = 18$mm, $r_1 = 10.8$mm to $R_1 = 17.8$mm, $r_1 = 10.68$mm while the ratio between larger and smaller ones is retained. This radius reduction induces slight resonance frequency mismatching between two single resonators at the overlapping frequency f_2. The results of simulation and measurement are shown in Figure 3.10 (a) and (b). This mismatching enables frequency tuning of the filtered peak. For this reason, using this couple structure with rotated probes, we proved frequency tuning of the coupled structure which can be applied to multiple index sensing.
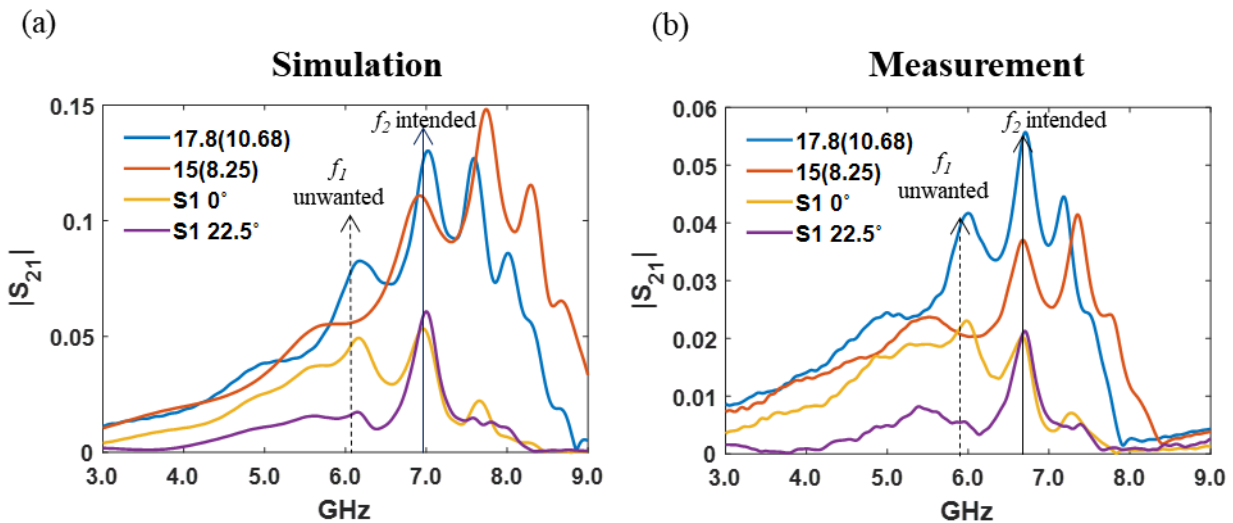
Figure 3.10 Coupled structure with Vernier effect with reduced larger resonator. In this figure, larger resonator is reduced from $R = 18$mm and $r = 10.8$mm to $R = 17.8$mm and $r = 10.68$mm compared to the Figure 3.9, while smaller resonator keeps its size. **(a)**, **(b)** are simulation and measurement results. We can find small mismatching at f_2 between hexapole resonance from smaller resonator and octupole resonance from larger resonator. Other than the reduced larger resonator, all the forms are same as Figure 3.9.

For sensing test, we took the structure used in Figure 3.10 and conducted experiments while changing sensing elements on the left resonator (fill factor of the sensing elements on the left is abbreviated as $f.f._1$) and fixing elements on the right resonator (denoted as $f.f._2$). We illustrated the situation of the measurement in Figure 3.11 (a). The left, middle and right columns in the figure correspond to the case where $f.f._2$ is fixed as 0, 0.6, 1. The results of the measurements are shown at Figure 3.11 (b) and we magnified the frequency range near the overlap. Below the graphs, Figure 3.11 (c) are analyses of the peaks in figure (b).

Firstly, we put a sensing element at only left resonator and measured while changing the $f.f._1$, shown in the left column. In this case, when $f.f._1 = 0.2$ corresponding to orange line in left column of figure (b), the peak shows largest S21 value and it is confirmed by the left analysis graph in Figure 3.11 (c). This results can be understood by illustration of Figure 3.11 (d). Blue lines correspond to the larger resonator, yellow lines to the smaller resonator and the purple line to the coupled structure. When $f.f._1 = 0$, in other words, there are no sensing elements on either resonators, resonance peaks of the two resonances (faint and bold blue line; orange line in left of the Figure 3.11 (d)) do not overlap because we intended the mismatching at Figure 3.10. When the $f.f._1$ increases, blue peak is red-shifted. In the meantime, when $f.f._1 = 0.2$ denoted as heavy blue color, these two peaks overlappe and the coupled structure denoted as purple curve shows the largest S21 value (heavy purple curve) . Secondly, after loading sensing material on the right with $f.f._2 = 0.6$ while changing $f.f._1$ similar to the first case, we measured again (middle column of Figure 3.11). In this case, when $f.f._1 = 0.4$, |S21| shows the largest value, as seen in the middle of Figure 3.11 (b) and (c). We will use the illustration of Figure 3.11 (d) again for an explanation. In the middle of the figure (d), due to the sensing element on right with $f.f._2 = 0.6$, the orange line is red-shifted from faint to thick color. So a blue line was required to further red-shift for resonance peak overlapping and this caused increased $f.f._1$ compared to the first case. Thirdly, we even put the sensing element on the right, whose fixed $f.f._2 = 1$ and the others are similar to former cases (right column). The resonance of the smaller resonator is shifted much more than first and second cases, thus overlapping occurs at even lower frequency compared to the first and second case with $f.f._1 = 0.8$.

Likewise, according to the these sensing elements, the tuning of resonance peak frequencies and intensities are possible in the coupled structure. Although these filtering effects are not quite remarkable according to the fill factor of the elements due to the inkjet printing method, if we fabricate the samples by other ways (e.g., PCB method), larger conductivity and sharp resonance peaks can be achieved. Then, resonane filtering and tuning would be conspicuous. If used cleaverly, this concept may enable multiple index sensing or complex signals such as logic gate.

Figure 3.11 Index sensing test using coupled structure with the Vernier effect. **(a)** Illustrations that explain experimental conditions according to the sensing elements. Arrangement of source and detectors is described, which are already introduced in Figure 3.9. In all cases, on right resonator, sensing elements are fixed with $f.f._2 = 0$ (left column) or 0.6 (middle column) or 1 (right column), while elements on left ($f.f._1$) are changing. **(b)** Results of sensing experiments. Frequency ranges are zoomed in near hexapole resonance. **(c)** Analysis of hexapole resonance peaks in (b). Left y-axis with black color represents resonance frequency, right y-axis with red color |S21| and x-axis $f.f._1$. Doted lines denote largest |S21| value for each cases. **(d)** Illustrations explaining the frequency shifts, where the largest intensity peaks occur in each case. Blue, orange, purple lines correspond to the larger, smaller resonator and coupled structure, respectively. For each case, bold lines correspond to where resonance peaks are overlapped.

4. Conclusion

In this thesis, we studied spoof LSPs. To comprehend spoof LSPs well, we designed and simulated the structures to observe what happen if the structures are changed. Then we fabricated a resonator using inkjet printer with Ag nanoparticle ink on paper. We found the proper annealing condition, which maximized conductivity of the printed samples. We measured the printed samples using monopole source and proved that the samples worked well by comparing to the simulation. Because the samples were large enough, it was easy to locate the source and detector at specific position. By rotating the probes, we converted the resonance peak into a dip, clarifying faint resonance. With this method, we realized spoof LSPs very easily, fast and affordably.

For the application of spoof LSP, we conducted sensing test. Sensing elements with different refractive indexes were obtained by adjusting fill factor using 3d printer. Increasing fill factor red-shifted resonances with decreasing or increasing $|S_{21}|$ value of peaks or dips. Finally, we studied coupled structures with Vernier effect and adopted rotating probes again to filter resonance peaks for sensing test. In this coupled structure, we showed resonance filtering and conducted sensing test with 2 sensing elements. We proved sensing ability of spoof LSPs and suggested double index sensing or signal generation concept.

For the future studies, using spoof LSPs, we plan to conduct real material (e.g., biomolecules) sensing. Because of its convenient manufacturing, simple inspections can be achieved. And using stimuli-responsive materials sensitive to the ambient condition, we will fabricate and study environment sensors.

5. Reference

[1]   S. A. Maier, *Plasmonics: fundamentals and applications*. Springer Science & Business Media, 2007.

[2]   W. L. Barnes, A. Dereux, and T. W. Ebbesen, "Surface plasmon subwavelength optics," *nature,* vol. 424, no. 6950, p. 824, 2003.

[3]   R. H. Ritchie, "Plasma losses by fast electrons in thin films," *Physical review,* vol. 106, no. 5, p. 874, 1957.

[4]   M. L. Juan, M. Righini, and R. Quidant, "Plasmon nano-optical tweezers," *Nature Photonics,* vol. 5, no. 6, pp. 349-356, 2011/06/01 2011, doi: 10.1038/nphoton.2011.56.

[5]   S. Kawata, Y. Inouye, and P. Verma, "Plasmonics for near-field nano-imaging and superlensing," *Nature photonics,* vol. 3, no. 7, p. 388, 2009.

[6]   A. Cattoni *et al.*, "λ3/1000 plasmonic nanocavities for biosensing fabricated by soft UV nanoimprint lithography," *Nano letters,* vol. 11, no. 9, pp. 3557-3563, 2011.

[7]   D. Rodrigo *et al.*, "Mid-infrared plasmonic biosensing with graphene," *Science,* vol. 349, no. 6244, pp. 165-168, 2015.

[8]   D. K. Gramotnev and S. I. Bozhevolnyi, "Plasmonics beyond the diffraction limit," *Nature photonics,* vol. 4, no. 2, p. 83, 2010.

[9]   M. Ozaki, J.-i. Kato, and S. Kawata, "Surface-plasmon holography with white-light illumination," *Science,* vol. 332, no. 6026, pp. 218-220, 2011.

[10]   A. Polman and H. A. Atwater, "Photonic design principles for ultrahigh-efficiency photovoltaics," *Nature materials,* vol. 11, no. 3, p. 174, 2012.

[11]   P. Biagioni, J.-S. Huang, and B. Hecht, "Nanoantennas for visible and infrared radiation," *Reports on Progress in Physics,* vol. 75, no. 2, p. 024402, 2012.

[12]   H. B. Jeon, P. V. Tsalu, and J. W. Ha, "Shape Effect on the Refractive Index Sensitivity at Localized Surface Plasmon Resonance Inflection Points of Single Gold Nanocubes with Vertices," *Scientific Reports,* vol. 9, no. 1, p. 13635, 2019/09/20 2019, doi: 10.1038/s41598-019-50032-3.

[13]   A. Kinkhabwala, Z. Yu, S. Fan, Y. Avlasevich, K. Müllen, and W. E. Moerner, "Large single-molecule fluorescence enhancements produced by a bowtie nanoantenna," *Nature Photonics,* vol. 3, no. 11, pp. 654-657, 2009/11/01 2009, doi: 10.1038/nphoton.2009.187.

[14]   F. Mastrotto *et al.*, "Polymer control of ligand display on gold nanoparticles for multimodal switchable cell targeting," vol. 47, no. 35, p. 9846, 2011, doi: 10.1039/c1cc12654g.

[15]   J. D. Jackson, "Classical electrodynamics," ed: AAPT, 1999.

[16]   J. Zenneck, "Propagation of plane EM waves along a plane conducting surface," *Ann. Phys.(Leipzig),* vol. 23, no. 1, p. 907, 1907.

[17]   C. Tiejun, D. Smith, and L. Ruopeng, "Metamaterials: theory, design and applications [M]," ed: New York: Springer, 2010.

[18]   J. Pendry, L. Martin-Moreno, and F. Garcia-Vidal, "Mimicking surface plasmons with structured surfaces," *science,* vol. 305, no. 5685, pp. 847-848, 2004.

[19]   F. Garcia-Vidal, L. Martin-Moreno, and J. Pendry, "Surfaces with holes in them: new plasmonic metamaterials," *Journal of optics A: Pure and applied optics,* vol. 7, no. 2, p. S97, 2005.

[20]   F. G. De Abajo and J. Sáenz, "Electromagnetic surface modes in structured perfect-conductor surfaces," *Physical review letters,* vol. 95, no. 23, p. 233901, 2005.

[21]   E. Hendry, A. P. Hibbins, and J. R. Sambles, "Importance of diffraction in determining the dispersion of designer surface plasmons," *Physical Review B,* vol. 78, no. 23, p. 235426, 2008.

[22]   M. Qiu, "Photonic band structures for surface waves on structured metal surfaces," *Optics express,* vol. 13, no. 19, pp. 7583-7588, 2005.

[23]   A. Fernandez-Dominguez, F. Garcia-Vidal, and L. Martin-Moreno, "Surface electromagnetic waves on structured perfectly conducting surfaces," *Structured surfaces as optical metamaterials,* pp. 232-266, 2011.

[24]   H.-H. Tang, Y. Tan, and P.-K. Liu, "Near-Field and Far-Field Directional Conversion of Spoof

Surface Plasmon Polaritons," *Scientific Reports,* vol. 6, no. 1, p. 33496, 2016/09/15 2016, doi: 10.1038/srep33496.

[25]   X. Shen, T. J. Cui, D. Martin-Cano, and F. J. Garcia-Vidal, "Conformal surface plasmons propagating on ultrathin and flexible films," *Proceedings of the National Academy of Sciences,* vol. 110, no. 1, pp. 40-45, 2013.

[26]   X. Gao *et al.*, "Ultrathin dual-band surface plasmonic polariton waveguide and frequency splitter in microwave frequencies," *Applied Physics Letters,* vol. 102, no. 15, p. 151912, 2013.

[27]   B. You, W.-J. Cheng, J.-Y. Lu, T.-A. Liu, and T. Hattori, "Terahertz plasmonic waveguides based on a microstructure of metal rod array," in *2015 40th International Conference on Infrared, Millimeter, and Terahertz waves (IRMMW-THz)*, 2015: IEEE, pp. 1-2.

[28]   M. A. Kats, D. Woolf, R. Blanchard, N. Yu, and F. Capasso, "Spoof plasmon analogue of metal-insulator-metal waveguides," *Optics express,* vol. 19, no. 16, pp. 14860-14870, 2011.

[29]   C. Han, Y. Chu, Z. Wang, and X. Zhao, "Spoof surface plasmonic waveguide devices with compact length and low-loss," *Journal of Applied Physics,* vol. 122, no. 12, p. 123301, 2017.

[30]   D. Woolf, M. A. Kats, and F. Capasso, "Spoof surface plasmon waveguide forces," *Optics letters,* vol. 39, no. 3, pp. 517-520, 2014.

[31]   X. Gao, L. Zhou, and T. J. Cui, "Odd-mode surface plasmon polaritons supported by complementary plasmonic metamaterial," *Scientific reports,* vol. 5, p. 9250, 2015.

[32]   X. Tian *et al.*, "Wireless body sensor networks based on metamaterial textiles," *Nature Electronics,* p. 1, 2019.

[33]   A. Pors, E. Moreno, L. Martin-Moreno, J. B. Pendry, and F. J. Garcia-Vidal, "Localized spoof plasmons arise while texturing closed surfaces," *Physical review letters,* vol. 108, no. 22, p. 223905, 2012.

[34]   P. A. Huidobro, A. I. Fernández-Domínguez, J. B. Pendry, L. Martin-Moreno, and F. J. Garcia-Vidal, *Spoof Surface Plasmon Metamaterials*. Cambridge University Press, 2018.

[35]   Z. Gao, L. Wu, F. Gao, Y. Luo, and B. Zhang, "Spoof plasmonics: from metamaterial concept to topological description," *Advanced Materials,* vol. 30, no. 31, p. 1706683, 2018.

[36]   P. A. Huidobro *et al.*, "Magnetic localized surface plasmons," *Physical Review X,* vol. 4, no. 2, p. 021003, 2014.

[37]   X. Shen and T. J. Cui, "Ultrathin plasmonic metamaterial for spoof localized surface plasmons," *Laser & Photonics Reviews,* vol. 8, no. 1, pp. 137-145, 2014.

[38]   Y. J. Zhou, Q. X. Xiao, and B. J. Yang, "Spoof localized surface plasmons on ultrathin textured MIM ring resonator with enhanced resonances," *Scientific reports,* vol. 5, p. 14819, 2015.

[39]   Z. Liao, A. I. Fernández-Domínguez, J. Zhang, S. A. Maier, T. J. Cui, and Y. Luo, "Homogenous metamaterial description of localized spoof plasmons in spiral geometries," *Acs Photonics,* vol. 3, no. 10, pp. 1768-1775, 2016.

[40]   B. J. Yang, Y. J. Zhou, and Q. X. Xiao, "Spoof localized surface plasmons in corrugated ring structures excited by microstrip line," *Optics express,* vol. 23, no. 16, pp. 21434-21442, 2015.

[41]   F. Gao, Z. Gao, Y. Zhang, X. Shi, Z. Yang, and B. Zhang, "Vertical transport of subwavelength localized surface electromagnetic modes," *Laser & Photonics Reviews,* vol. 9, no. 5, pp. 571-576, 2015.

[42]   Z. Liao, G. Q. Luo, B. G. Cai, B. C. Pan, and W. H. Cao, "Subwavelength negative-index waveguiding enabled by coupled spoof magnetic localized surface plasmons," *Photonics Research,* vol. 7, no. 3, pp. 274-282, 2019.

[43]   J. Zhang, Z. Liao, Y. Luo, X. Shen, S. A. Maier, and T. J. Cui, "Spoof plasmon hybridization," *Laser & Photonics Reviews,* vol. 11, no. 1, p. 1600191, 2017.

[44]   Z. Gao, F. Gao, Y. Zhang, H. Xu, Y. Luo, and B. Zhang, "Forward/Backward Switching of Plasmonic Wave Propagation Using Sign-Reversal Coupling," *Advanced Materials,* vol. 29, no. 26, p. 1700018, 2017.

[45]   F. Gao, Z. Gao, Y. Luo, and B. Zhang, "Invisibility Dips of Near-Field Energy Transport in a Spoof Plasmonic Metadimer," *Advanced Functional Materials,* vol. 26, no. 45, pp. 8307-8312, 2016.

[46]   Z. Liao, Y. Luo, A. I. Fernández-Domínguez, X. Shen, S. A. Maier, and T. J. Cui, "High-order

localized spoof surface plasmon resonances and experimental verifications," *Scientific reports,* vol. 5, p. 9590, 2015.

[47] Z. Gao, F. Gao, H. Xu, Y. Zhang, and B. Zhang, "Localized spoof surface plasmons in textured open metal surfaces," *Optics letters,* vol. 41, no. 10, pp. 2181-2184, 2016.

[48] B. Sun and Y. Yu, "Destroyed-toroidal-localized-spoof-plasmon-induced Fano resonance in plasmonic metamaterial for self-reference plasmonic sensor," *Journal of Physics D: Applied Physics,* vol. 52, no. 24, p. 245001, 2019.

[49] R. L. Shao, Y. J. Zhou, and L. Yang, "Quarter-mode spoof plasmonic resonator for a microfluidic chemical sensor," *Applied optics,* vol. 57, no. 28, pp. 8472-8477, 2018.

[50] J. Cai, Y. J. Zhou, Y. Zhang, and Q. Y. Li, "Gain-assisted ultra-high-Q spoof plasmonic resonator for the sensing of polar liquids," *Optics express,* vol. 26, no. 19, pp. 25460-25470, 2018.

[51] B. Sun and Y. Yu, "Double toroidal spoof localized surface plasmon resonance excited by two types of coupling mechanisms," *Optics letters,* vol. 44, no. 6, pp. 1444-1447, 2019.

[52] W. Xiang, K. Zheng, and X. S. Shen, *5G mobile communications*. Springer, 2016.

[53] D. Lee, Y. Seo, and S. Lim, "Dipole-and loop-mode switchable origami paper antenna," *Microwave and Optical Technology Letters,* vol. 58, no. 3, pp. 668-672, 2016.

[54] N. E. Sanjana and S. B. Fuller, "A fast flexible ink-jet printing method for patterning dissociated neurons in culture," *Journal of neuroscience methods,* vol. 136, no. 2, pp. 151-163, 2004.

[55] S. A. Nauroze, L. S. Novelino, M. M. Tentzeris, and G. H. Paulino, "Continuous-range tunable multilayer frequency-selective surfaces using origami and inkjet printing," *Proceedings of the National Academy of Sciences,* vol. 115, no. 52, pp. 13210-13215, 2018.

[56] P. Azuelos *et al.*, "Theoretical investigation of Vernier effect based sensors with hybrid porous silicon-polymer optical waveguides," *Journal of Applied Physics,* vol. 121, no. 14, p. 144501, 2017.

[57] V. Zamora, P. Lützow, M. Weiland, and D. Pergande, "A highly sensitive refractometric sensor based on cascaded SiN microring resonators," *Sensors,* vol. 13, no. 11, pp. 14601-14610, 2013.

[58] P. Azuelos *et al.*, "High sensitivity optical biosensor based on polymer materials and using the Vernier effect," *Optics express,* vol. 25, no. 24, pp. 30799-30806, 2017.

[59] K. Saleh *et al.*, "Photonic Generation of High Power, Ultrastable Microwave Signals by Vernier Effect in a Femtosecond Laser Frequency Comb," *Scientific reports,* vol. 8, no. 1, p. 1997, 2018.

[60] P. Drude, "Zur Elektronentheorie der Metalle; II. Teil. Galvanomagnetische und thermomagnetische Effecte," *Annalen der Physik,* vol. 308, no. 11, pp. 369-402, 1900, doi: 10.1002/andp.19003081102.

[61] N. Kinsey, C. DeVault, A. Boltasseva, and V. M. Shalaev, "Near-zero-index materials for photonics," *Nature Reviews Materials,* vol. 4, no. 12, pp. 742-760, 2019/12/01 2019, doi: 10.1038/s41578-019-0133-0.

[62] Z. Liao, X. Shen, B. C. Pan, J. Zhao, Y. Luo, and T. J. Cui, "Combined System for Efficient Excitation and Capture of LSP Resonances and Flexible Control of SPP Transmissions," *ACS Photonics,* vol. 2, no. 6, pp. 738-743, 2015/06/17 2015, doi: 10.1021/acsphotonics.5b00096.

[63] C. Jang, J.-K. Park, H.-J. Lee, G.-H. Yun, and J.-G. Yook, "Temperature-corrected fluidic glucose sensor based on microwave resonator," *Sensors,* vol. 18, no. 11, p. 3850, 2018.

[64] Y. Zhang, J. Zhao, J. Cao, and B. Mao, "Microwave metamaterial absorber for non-destructive sensing applications of grain," *Sensors,* vol. 18, no. 6, p. 1912, 2018.

[65] Z. Liao, B. C. Pan, X. Shen, and T. J. Cui, "Multiple Fano resonances in spoof localized surface plasmons," *Optics express,* vol. 22, no. 13, pp. 15710-15717, 2014.

[66] Y. Huang, J. Zhang, T. J. Cui, Z. Liao, and D. H. Zhang, "Revealing the physical mechanisms behind large field enhancement in hybrid spoof plasmonic systems," *JOSA B,* vol. 35, no. 2, pp. 396-401, 2018.